

Realization of a Laser Calibration System for the MicroBooNE Neutrino Experiment

Masterarbeit der Philosophisch-naturwissenschaftlichen Fakultät
der Universität Bern

vorgelegt von

Matthias Lüthi

2014

Leiter der Arbeit

Prof. Dr. Antonio Ereditato

PD Dr. Igor Kreslo

Albert Einstein Center for Fundamental Physics
Laboratory for High Energy Physics
Physikalisches Institut
University of Bern, Switzerland

Abstract

The MicroBooNE neutrino oscillation experiment is based on a liquid argon time projection chamber (LAr TPC) situated in a neutrino beam at Fermilab in the USA. The TPC drift field is anticipated to be altered by the build up of space charge caused by the constant ionisation of the liquid argon by cosmic rays. Therefore, a calibration of the drift field is necessary for precise particle track reconstruction. A calibration map of the drift field can be obtained by providing a number of straight ionization tracks by a UV-laser beams and scanning the full detector volume.

The scope of this master thesis is to establish the performance and to characterise a laser calibration system aimed for the installation in the MicroBooNE detector. The laser calibration system was tested in a prototype LAr TPC, in the framework of LAr TPC R&D efforts at LHEP (Laboratory for High Energy Physics). Fully automated scans of the detector volume were performed. Identified parameters include the measurement accuracy of the mirror employed in the liquid argon of $\sigma_{vertical} = 10.3''$ and $\sigma_{horizontal} = 3.2''$ and the scanning speed $v_{vertical} = 2s/\circ$ and $v_{horizontal} = 2.6s/\circ$. The necessity for laser beam energy modulation was identified. In the presented setup a minimal resolvable field distortion of 5% was found. Furthermore, a dataset for future performance tests of field reconstruction algorithms was obtained. By comparing the precise physical laser beam position in the detector and the position of the reconstructed track allows to correct for space charge and miscalibration effects. The systematic uncertainty in the track position measurement can be reduced with this procedure from 10 cm down to millimetres.

Contents

Contents	iv
List of Figures	vii
1 Introduction	1
2 Short-Baseline Neutrino Oscillation	3
2.1 Neutrino Oscillation Searches at High Δm^2	3
2.2 The MicroBooNE Experiment	7
3 Working Principle of a Liquid Argon Time Projection Chamber	11
3.1 General Working Principle	11
3.2 Liquid Argon as Detector Medium	13
3.3 Laser Calibration System	20
4 Experimental Setup	25
4.1 Cryogenic Environment	25
4.2 Time Projection Chamber	27
4.3 Laser Calibration System	30
5 Experimental Results	35
5.1 Test of the Time Projection Chamber	35
5.2 Test of the Laser Feedthrough	37
5.3 Tests of the Laser Calibration System	39
5.4 Analysis of Collected Laser Tracks	46
5.5 Drift Speed Measurement	48
5.6 Purity Measurement	48
5.7 Outlook	51
6 Conclusions	53
A Photographs of the Setup	55
Bibliography	59
Acknowledgements	59

List of Figures

2.1	Expansion of the three neutrino mixing model.	4
2.2	Neutrino low energy excess observed in MiniBooNE.	6
2.3	LSND and MiniBooNE two-neutrino oscillation results.	7
2.4	CAD drawing of the MicroBooNE detector.	9
3.1	Signal generation on the wireplane in a TPC.	12
3.2	Illustration of the relevant processes in a TPC.	14
3.3	Primary scintillation time evolution for liquid argon.	17
3.4	Charge and light yield vs electric field for liquid argon.	18
3.5	Drift velocity vs electric field for liquid argon.	19
3.6	Illustration of field distortion effect.	21
3.7	Space charge effect simulation for MicroBooNE.	22
3.8	Energy levels for gaseous and liquid argon	23
4.1	Vacuum and cryogenic system.	26
4.2	Field shaping rings and configuration	28
4.3	Schematic of DAQ system	29
4.4	Diagram of laser optics table.	31
4.5	CAD drawing of the feedthrough and the mirror support structure.	32
4.6	Motor and encoder control components.	33
4.7	Sketch of laser path in the TPC.	33
5.1	Wire signals.	36
5.2	Muon track.	37
5.3	Electromagnetic shower.	38
5.4	Laser ionization track in the detector.	39
5.5	Laser beam hitting cathode.	39
5.6	Recorded position and laser energy for a detector scan.	41
5.7	Reflectivity vs angle of incidence for UV-mirror.	43
5.8	Simulation of the field strength and field lines	44
5.9	Laser track in full laser calibration system.	45
5.10	Laser track with shortened rings 3 and 4.	45
5.11	Laser track parallel to readout plane	46
5.12	Collected laser track for homogenous and distorted field configuration.	47
5.13	Measurement of the electron drift speed.	49
5.14	Example event display for purity measurement.	50
5.15	Wire signals and attenuation analysis.	50
A.1	Photograph of the optical table.	55

A.2 Photograph of the laser feedthrough.	56
A.3 Photograph of the detector.	57

Chapter 1

Introduction

After Pauli postulated the neutrino to fulfil conservation of energy and angular momentum in β -decays in 1930, almost 25 years passed until Cowan and Reines provided experimental proof for the existence of neutrinos. Since then many other experiments were conducted to investigate neutrino properties, but still open questions exist. A decade ago strong evidence was found for neutrino flavour oscillation in the angular distribution of atmospheric neutrinos. Later the oscillation model was confirmed with measurements of neutrinos produced in thermonuclear reaction in the solar core. The picture was completed by the exposure of detectors to man-made neutrinos (accelerators and reactors). All this experimental evidence leads to the conclusion that neutrinos are massive particles, however oscillation experiments are unable to provide information about the absolute masses. Experiments carefully measuring kinematics of the β -decay have so far set upper limits to absolute neutrino masses.

Great amount of effort is being made in measuring precisely the mixing angles, the mass difference and hierarchy and a possible CP violating phase which characterise neutrino oscillation. A detector employed for this purpose should fulfil the following requirements:

1. Large target mass because of low neutrino cross section.
2. Charged particle identification (e, μ) to distinguish neutral and charged current neutrino interactions.
3. Measurement of the energy (calorimetry) and trajectory (imaging) of the outgoing particles to determine kinematic variables.
4. Measurement of the total energy of outgoing hadrons to infer the neutrino energy.

A liquid argon time projection chamber (LAr TPC), first proposed in 1977 [34], incorporates all these properties. The high density of 1.4 kg/l enhances the target mass, at the cost of cryogenic operation ($T_{liquid} = 87\text{ K}$ at 1 bar). Liquid argon is not only the target but also the detection medium, charged particles will ionize the liquid argon and the so created electrons are drifted to a readout plane. This provides both calorimetric

information by means of the amount of collected charge and imaging capabilities by the fine-grain readout of the electrons at the end of the drift path. Today the largest LAr TPCs have active masses in the range of hundred tons, future experiments are planned to operate with hundreds of kilotons of liquid argon in a neutrino beam. These detectors promise a rich scientific outcome and a significant improvement in sensitivity for neutrino oscillation parameters.

Several challenges arise when scaling a LAr TPC to ton or even multiton active target. For precise track reconstruction a well known electric field (closely linked to the drift velocity of electrons) is essential in a TPC, a linear field is preferred due to the simplification in reconstruction. However the field can be altered by several processes: the build up of space charge due to constant ionisation of LAr by cosmic particles, uncertainties in the alignment of the detector structure and possible temperature variations affecting the drift speed of electrons. A calibration map of the electric field can be obtained by imitating straight particle tracks by the introduction of a laser beam into the TPC. These straight tracks will be bent in the presence of the above discussed effects. By comparing the known physical and recorded trajectory in the detector a drift field calibration map can be constructed.

The assembly and evaluation of such a laser calibration system aimed for operation on MicroBooNE (Micro Booster Neutrino Experiment), a short-baseline neutrino experiment, is the scope of this master thesis. The system is designed and built at LHEP (Laboratory for High Energy Physics) in the framework of R&D in LAr TPC technology. In chapter 2 a short introduction to MicroBooNE is given, followed by a discussion of LAr TPC working principles in chapter 3. Chapter 4 describes the experimental setup in detail and in chapter 5 obtained results are presented. At last in chapter 6 the thesis is summarised.

Chapter 2

Short-Baseline Neutrino Oscillation

MicroBooNE is a short baseline neutrino experiment in the Booster Neutrino Beam (BNB) at Fermilab, it will investigate the low energy electron-like excess observed in MiniBooNE. Furthermore detailed studies of neutrino cross sections will be performed. The detector is a liquid argon time projection chamber (LAr TPC) chosen for its fine grain tracking and the calorimetry, which allow for high precision particle identification. Additionally the experiment is a LAr TPC technology test with regards to future upscaling for long baseline neutrino experiments.

2.1 Neutrino Oscillation Searches at High Δm^2

The hypothesis of neutrino oscillation, where neutrinos of a certain flavour in a beam evolve into a different flavour, has been put on solid experimental ground in the past 15 years. Based on this observations a phenomenological model including three finite masses and a (3×3) mixing matrix connecting three flavour states (ν_e , ν_μ and ν_τ) with three mass states (ν_1 , ν_1 and ν_2) has been introduced [19]. In this accepted picture two mass splittings are measurable by oscillation experiments with $\Delta m_{21}^2 = 7.50 \pm 0.185 \times 10^{-5}$ eV 2 and $\Delta m_{32}^2 = 2.47^{+0.069}_{-0.067} \times 10^{-7}$ eV 2 . However, among others, experiments located very close to the neutrino source (called short baseline neutrino experiments) have provided evidence for oscillations connected to a mass splitting $\Delta m^2 \approx 1$ eV 2 , which are incompatible with the three neutrino model. A way to accommodate this higher mass splitting oscillations in the established model is to introduce one or more non-interacting (sterile) neutrino states. The sterility to other interactions is necessary to exclude possible interference with the measurement of the number of light neutrino types of $N_\nu = 2.9840 \pm 0.0082$ [35] determined by LEP experiments through the measurement of the invisible width of the Z boson.

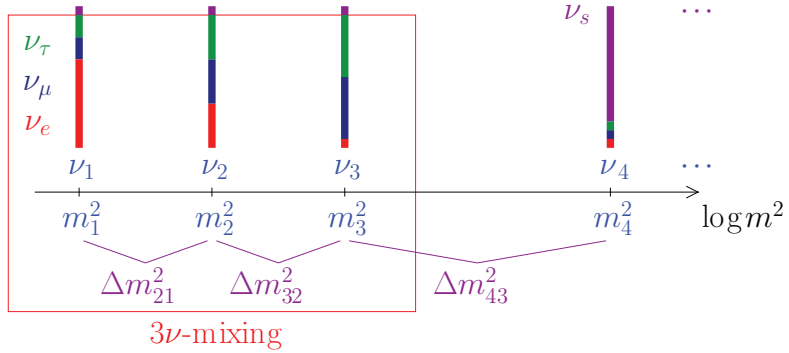


FIGURE 2.1: Expansion of the three active neutrino mixing model (red box) by the addition of one or more relatively heavy sterile neutrino. Modified from [16].

The lowest order model of neutrino oscillation involves two flavour states ν_e and ν_μ which are linked to the two mass states ν_1 and ν_1 via a mixing matrix analogous to a rotation matrix. Here the neutrino flavour states are described in terms of mass states in the following way:

$$|\nu_e\rangle = \cos(\theta) |\nu_1\rangle + \sin(\theta) |\nu_2\rangle \quad (2.1)$$

and

$$|\nu_\mu\rangle = -\sin(\theta) |\nu_1\rangle + \cos(\theta) |\nu_2\rangle, \quad (2.2)$$

with the known mixing angle θ . With this description of the two states the probability of flavour change after a travel distance L in meters and neutrino energy E in MeV with mass splitting $\Delta m_{21}^2 = m_2^2 - m_1^2$ is given by

$$P = \sin^2(2\theta) \sin^2(1.27\Delta m^2(L/E)). \quad (2.3)$$

Neutrino beam energies lie typically in the region between few MeV and few GeV, therefore to be sensitive for oscillations in the the region of $\Delta m^2 \approx 1 \text{ eV}^2$ one has to choose the baseline L in the region of few hundred meters.

Any data obtained in a single short baseline oscillation experiment may well be fitted to a two oscillation model. But combining several experimental data will need the addition of neutrino flavours, as demonstrated in the model of three active neutrino mixing. How to extend this model to incorporate additional sterile neutrino flavours is described extensively in [9]. The simplest model adds one sterile neutrino ν_s (3+1 model) that can mix with the three other active flavours. A schematic representation of the mass states is shown in Figure 2.1. Consequently a (4×4) mixing matrix is necessary to describe oscillations in a 3+1 model, including the known matrix elements of the active mixing.

This matrix connects the four mass states with the four flavour states:

$$\begin{pmatrix} \nu_e \\ \nu_\mu \\ \nu_\tau \\ \nu_s \end{pmatrix} = \begin{pmatrix} U_{e1} & U_{e2} & U_{e3} & U_{e4} \\ U_{\mu 1} & U_{\mu 2} & U_{\mu 3} & U_{\mu 4} \\ U_{\tau 1} & U_{\tau 2} & U_{\tau 3} & U_{\tau 4} \\ U_{s1} & U_{s2} & U_{s3} & U_{s4} \end{pmatrix} \begin{pmatrix} \nu_1 \\ \nu_2 \\ \nu_3 \\ \nu_4 \end{pmatrix}. \quad (2.4)$$

Mixing parameters in the active sector of the matrix are highly constrained by several measurements [19]. Assuming that $\Delta m_{21}^2 \approx \Delta m_{32}^2 = 0$, justified by the assumption that the sterile neutrino mass is much larger than the masses of the active neutrino, and $|U_{\tau 4}|$ is negligible leads to a simplification of the 3+1 model to a two neutrino oscillation. These assumptions are known as the short-baseline-assumptions. The probability of $\nu_\mu \rightarrow \nu_e$ appearance P_{app} reduces to Equation 2.3 where $\sin^2(2\theta)$ is given by

$$\sin^2(2\theta_{e\mu}) = 4U_{e4}^2 U_{\mu 4}^2. \quad (2.5)$$

The probability of disappearance ($\nu_\mu \rightarrow \nu_s$ or $\nu_e \rightarrow \nu_s$) is given by $P_{dis} = 1 - P$ where P is given by equation 2.3 and

$$\sin^2(2\theta_{\mu\mu}) = 4U_{\mu 4}^2(1 - U_{\mu 4}^2) \quad (\mu \text{ flavour}), \quad (2.6)$$

$$\sin^2(2\theta_{ee}) = 4U_{e4}^2(1 - U_{e4}^2) \quad (e \text{ flavour}). \quad (2.7)$$

In the same way the model can be extended with two or more sterile neutrinos. Current experimental data fit poorly within a 3+1 model, hence the introduction of a 3+2 model is motivated. In the following two short baseline neutrino oscillation experiments are discussed, namely LSND and MiniBooNE, which motivate the design and construction of the MicroBooNE experiment.

The LSND experiment was a liquid scintillator experiment at the Los Alamos National Laboratory which was exposed to a neutrino beam produced by protons impinged on a target producing pion decay at rest $\pi^+ \rightarrow \nu_\mu \mu^+$ followed by $\mu^+ \rightarrow e^+ \nu_e \bar{\nu}_\mu$ [6]. As a detector a cylindrical tank (8.3 m long and 5.7 m in diameter) was filled with liquid scintillator, the inner surface was covered by 1220 photomultipliers. The detector was located 29.8 m downstream of the beam. In the liquid scintillator detector the appearance of a $\bar{\nu}_e$ from possible $\bar{\nu}_\mu \rightarrow \bar{\nu}_e$ oscillation could interact via inverse β -decay $\bar{\nu}_e p \rightarrow e^+ n$ followed by a prompt positron and a correlated γ from neutron capture. The Cherenkov ring was used to determine the energy and angle of the outgoing positron. Only neutral current neutrino interactions were possible in the detector, since the neutrino energy was too low for charged current interactions. A cosmic veto system was installed around the detector to suppress background events. An excess over the expected background of $87.9 \pm 22.4 \pm 6.0$ events has been measured [2]. The found data was fitted to a two neutrino appearance model according to Equation 2.3 by maximum likelihood method. The allowed region of $\sin^2(2\theta)$ and Δm^2 for the recorded data is shown in Figure 2.3.

As a successor of LSND the MiniBooNE experiment was planned to investigate and con-

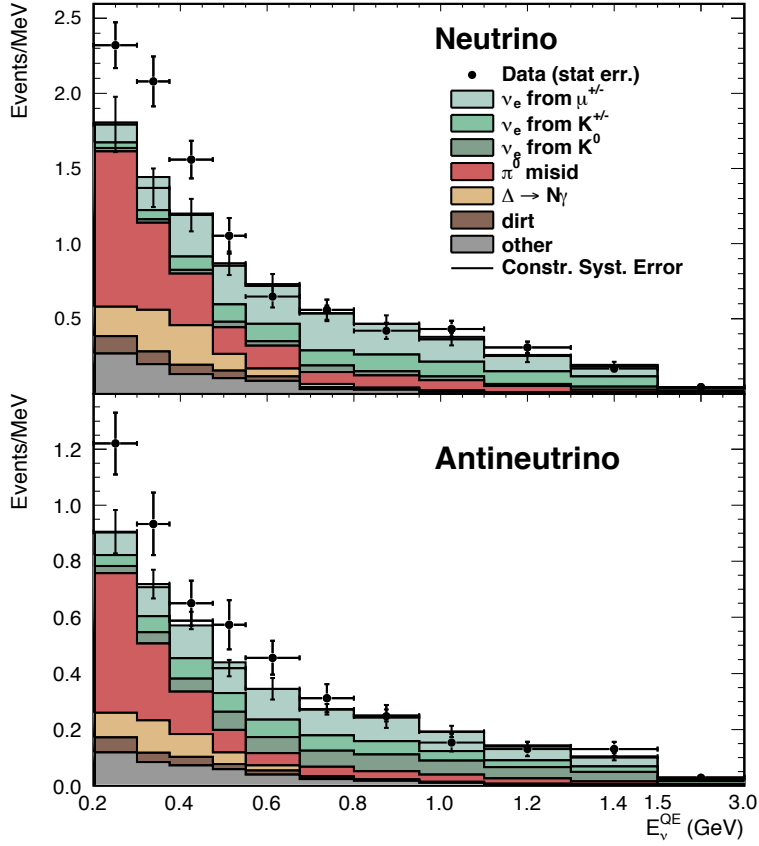


FIGURE 2.2: Dots indicate the measured MiniBooNE neutrino quasi elastic energy E_ν^{QE} distribution for electron neutrinos (top) and antineutrinos (bottom). The coloured histograms show the expected background. From [4].

firm the found oscillation parameter space in LSND. As a neutrino source a conventional neutrino beam, where protons hit a target producing mesons which decay in flight into muon (anti-)neutrinos, was employed at Fermilab. The beam could be switched from neutrino to antineutrino mode by selecting different mesons for the decay. Mineral oil was used as a detector medium in which most of the final state particles in neutrino interactions produce Cherenkov light. The oil was enclosed in a cylindrical vessel with 5 m radius and located 541 m away from the neutrino source. A photomultiplier array covering the inner spherical surface of the detector is used to identify the signature of a neutrino interactions [3]. The ν_e ($\bar{\nu}_e$) appearance signature was detected via $\nu_e n \rightarrow e^- p$ ($\bar{\nu}_e p \rightarrow e^+ n$), for which the Cherenkov ring of the electron (positron) was used to reconstruct the neutrino (antineutrino) energy. Within the detector no discrimination between photons and electrons is possible, since both interactions in the oil produce one single Cherenkov ring. The so recorded energy distribution was compared to the estimated background to identify oscillation signals. A total excess of 162 ± 47.8 (neutrino) and 78.4 ± 28.5 (antineutrino) events compared to estimated background could be identified in the measurement period between 2002 and 2012. Figure 2.2 shows the recorded

(anti-)neutrino energy distribution. The dataset can be fitted to a two-oscillation model, in which the oscillation probability is given by Equation 2.3, for both modes. Figure 2.3 shows the allowed regions for the parameters $\sin^2(2\theta)$ and Δm^2 for different confidence levels. In neutrino mode the allowed region is shifted toward lower Δm^2 compared to the LSND signal, whereas in antineutrino mode the MiniBooNE region is consistent with LSND.

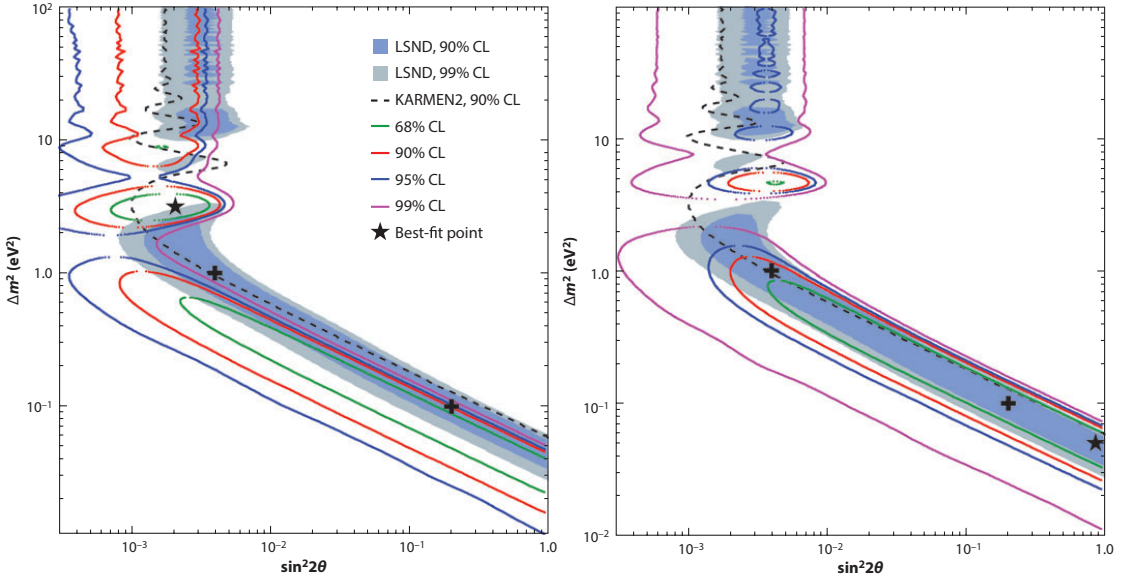


FIGURE 2.3: MiniBooNE allowed regions for the two-neutrino model in neutrino (left) and anti-neutrino (right) mode for different CL (coloured lines). Shaded regions indicate the allowed regions determined from the LSND measurements. Plot from [4].

In addition to the two discussed neutrino beam experiments, reactor based experiments have provided additional positive observation of high- Δm^2 neutrino oscillation [25]. To date the observed disappearance signal according to Equation 2.6 and 2.7 pose discrepancies when compared to appearance signals. Global fits to all available data poorly agree within a 3+1 model, the introduction of a 3+2 model improves the compatibility between measurements. A detailed discussion of 3+2 and 3+3 model fits to global experimental data can be found in [1], which is also recommended for further reading. The sterile neutrino hypothesis is far from being confirmed and new experiments are presently being constructed to explore the found signals and discrepancies.

2.2 The MicroBooNE Experiment

Motivated by the finding of high- Δm^2 neutrino oscillation, discussed in the previous section, an experiment investigating the signals observed in MiniBooNE is currently under way. Only 25 meters away from the MiniBooNE detector site, the MicroBooNE experiment will measure neutrino signals in the BNB (Booster Neutrino Beam) identical to

the beam used in MiniBooNE. The employed detector technology is a liquid argon time projection chamber (LAr TPC), which allows fine grain particle tracking. Furthermore differentiation between electron and photon is possible due to different apparent ionization rate at the beginning of their trajectory in liquid argon. The ability to distinguish between photon and electron is a significant improvement over the preceding MiniBooNE experiment and will determine the origin of the low-energy neutrino excess seen in MiniBooNE (see Figure 2.2) to be either from electrons or photons. The operation time will allow to identify either one of the excess origins with a 4σ (photons) to 5σ (electrons) significance. The low energy excess is not understood within current theoretical knowledge, hence understanding the source of it is one of the primary goals of MicroBooNE. Additionally, in contrast to MiniBooNE, background to single photon interactions, such as neutral current π^0 production, can efficiently be identified and rejected. These effects are the main contribution to the background of MiniBooNE in the low energy excess region. MicroBooNE will measure neutral and charged current quasi-elastic neutrino interactions (approximately 130000 expected events) in the LAr TPC including the observation of recoil nucleons. This ability will help to improve the current knowledge of neutrino cross section measurements. Finally, the MicroBooNE experiment is embedded into the strategy of neutrino oscillation research, by representing a first full scale test of a LAr TPC in a high intensity neutrino beam. This test includes the cryogenic environment, liquid argon purity, TPC design, cryogenic electronics, experiment operation and reconstruction software. The obtained experience with MicroBooNE will be valuable for the further upscaling of LAr TPCs.

The MicroBooNE LAr TPC has a rectangular shape situated in a cylindric single-walled cryostat, the active volume ($2.3\text{ m} \times 2.5\text{ m} \times 10\text{ m}$) will include 60 tons of liquid argon. The electric drift field is applied horizontally, on one side of the detector three wire-planes with a wire pitch of 3 mm are installed, resulting in 8256 wire readout channels. Thirty-two 8" photomultiplier tubes will be installed behind the wireplane for recording scintillation light. Figure 2.4 shows a CAD drawing of the MicroBooNE detector. For data acquisition of the wire signals a cold pre-amplifier followed by 12-bit analog-digital converter are foreseen. In a similar way the photomultiplier signal will be acquired. Offline event analysis, reconstruction and simulations will utilise LArSoft, a general purpose software package for LAr TPCs. Because of the detectors surface location, a constant penetration by particles produced in the upper atmosphere will be present. This results in approximately 6 to 10 cosmic events in every beam trigger window. The high intensity neutrino beam will be provided by the existing Fermilab Booster Neutrino Beam (BNB), to achieve the sensitivity for the proposed physics goals in total 6.6×10^{20} protons on target are necessary. In the technical design report [8] of the MicroBooNE collaboration a more detailed description of the physical goals and the planned detector properties is given.

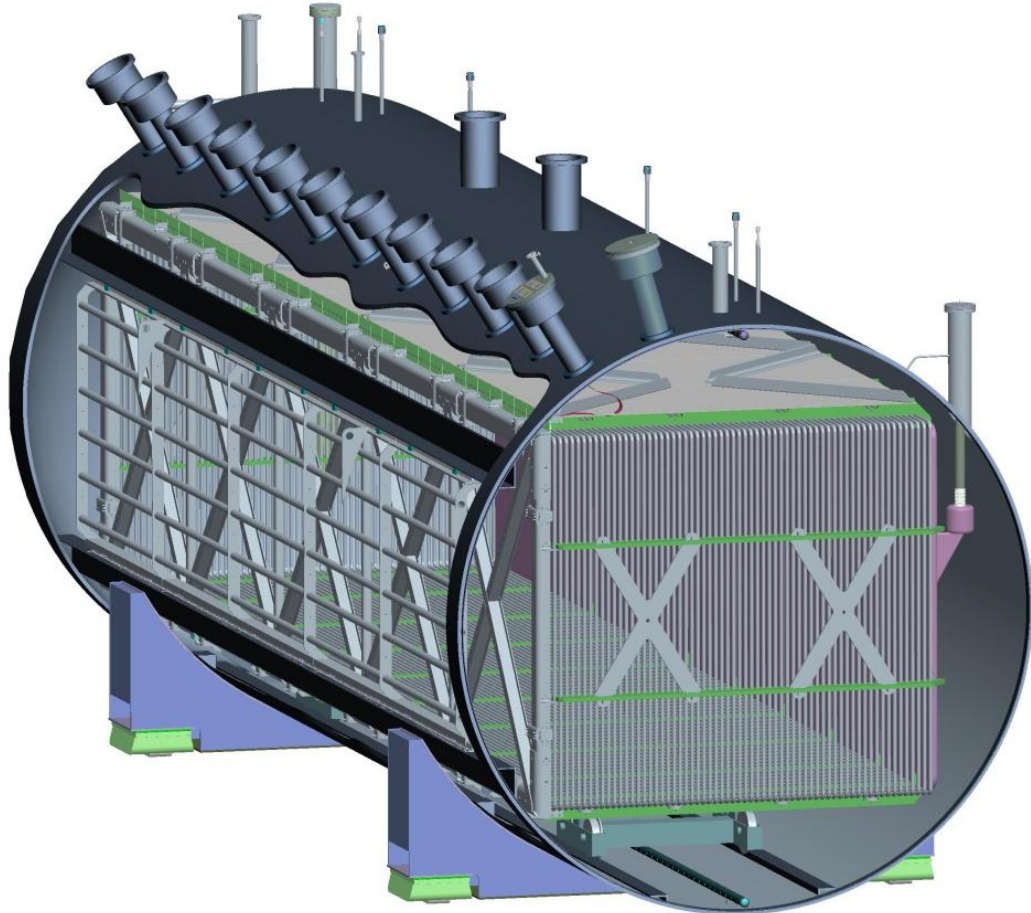


FIGURE 2.4: A CAD drawing of the MicroBooNE detector, neutrinos will enter from the front. The cathode is located at the very right, followed by field shaping rings towards the very left where the readout wires mark the end of the detector. In front of the wireplanes the photomultiplier support structure is visible. Drawing from [8].

Chapter 3

Working Principle of a Liquid Argon Time Projection Chamber

In this chapter an introduction to the working principle of liquid argon time projection chambers (LAr TPC) is given. This includes the general principle behind all TPCs as well as the special characteristics of liquid argon as target medium. Additionally the laser calibration system used to measure the electric field uniformity present inside the LAr TPC is presented.

3.1 General Working Principle

In 1970 Dave Nygren [24] proposed the use of a time projection chamber (TPC) for the PEP detector at SLAC, enabling particle tracking and measuring the specific energy loss (dE/dx) in the same detector volume. A charged particle traversing the active volume of an TPC will ionise the detection medium along its path. To prevent the ions and electrons to recombine an electric field is applied. The uniform electric field forces the electrons to drift along the field lines, maintaining the intrinsic particle track.

Spatial resolution is obtained by spanning two wire meshes perpendicular to each other at one end of the detector (x-y plane). Here the electric field is shaped such that the drifting electrons will induce a current on the inner wireplane and will be solely collected at the outer wireplane. The signals of the wireplanes are read out simultaneously allowing to determine the relative arrival times. This relative timing information enables the reconstruction of the particle track in the detector, Figure 3.1 illustrates the described procedure. During the drift path electrons can attach to electronegative impurities present in the detector, reducing the final signal strength. Hence the amount of electronegative impurities must be held at a very low level. With this scheme only relative particle tracks, with respect to an arbitrary readout time, are resolved. This means that one has no information about the absolute z-position of the particle track along the

drift field, but only a relative track somewhere inside the detector is known. Measuring the time elapsed between the wire signals and the actual transition of the particle will resolve this ambiguity if the drift speed of the electrons is known. For this purpose scintillation light produced by the particle traveling through the detector medium, which is assumed to be instantaneous compared to the drift time of the electrons, is recorded and used to absolutely position the ionization track inside the detector.

The described process of ionization and electron drift is generic to all TPCs, other parameters such as size, electron drift velocity, wireplane orientation, detector medium and many more may vary according to the needs of a particular experiment. In the following sections the focus is held on the use of liquid argon as a detector medium, but most of the described processes are also applicable on other choices of detector media, especially other noble gases.

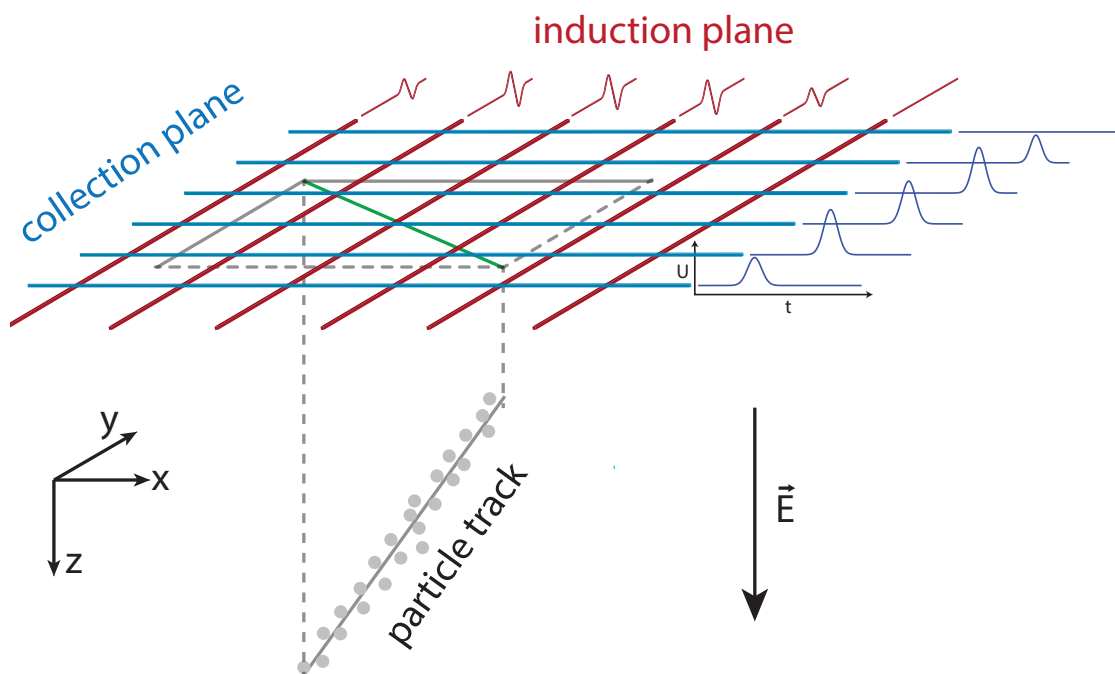


FIGURE 3.1: Generation of signals on the lower induction (red) and upper collection (blue) wireplane induced by electrons drifted to the wireplane. The green line represents the projected particle track onto the wireplanes. Signals formed on the wires are shifted relative in time by the later arrival time due to the longer drift distance (time) inside the detector.

Property	Value
Atomic Number	18
Atomic weight	39.94 u
Atomic diameter	3.42 Å
Radiation length	14.2 cm
Absorption length	83.6 cm
Molières Radius	10.1 cm
Critical energy for electrons	30.5 MeV
dE/dx for minimum ionizing particle	2.1 MeV/cm
Energy to produce an electron-ion pair	23.3 eV
Fano factor	0.107
Dielectric constant	1.6
Electron mobility	0.048 m ² V ⁻¹ s ⁻¹
Ion mobility	0.016 · 10 ⁻⁵ m ² V ⁻¹ s ⁻¹

TABLE 3.1: Liquid argon properties from [39].

3.2 Liquid Argon as Detector Medium

Table 3.1 summarises the chemical and physical properties of liquid argon. The high density of liquid argon allows for high efficiencies in detecting weakly interacting particles in a relatively small volume. The radiation length of 14.2 cm as well as the absorption length of 83.6 cm make liquid argon a favourable medium for calorimetry. Furthermore the energy needed to produce an electron ion pair converts to an electronic signal that can be detected. Combining the measurement of deposited energy (via ionization) with the spatial resolution of tracks allows for particle identification. In Figure 3.2 a schematic sequence of the processes inside the detector is given. These processes will be described in the following sections.

Particles passing through a media will lose energy through several different possible processes, namely pair production, Bremsstrahlung, Compton scattering, Cherenkov radiation and ionisation. A charged particle, under the assumption that the mass of the traversing particle is much higher than the mass of the electron ($M_{\text{particle}} \gg m_e$), will lose energy mainly through elastic collisions with electrons. The average energy deposited along a track of unit length is described by the Bethe-Bloch formula (see [13] for a detailed discussion). In liquid argon a minimum ionizing particle deposits a mean energy of 2.1 MeV/cm.

This energy lost by the incident particle is transferred to the argon atoms as ionization and excitation. The former process removes an electron from the atom leaving behind a positively charged ion and an electron (electron-ion pair). This electron may have sufficient kinetic energy to further ionize argon atoms. Most of the so formed argon ions will form argon excimer molecules. The latter process will rise the energy level of

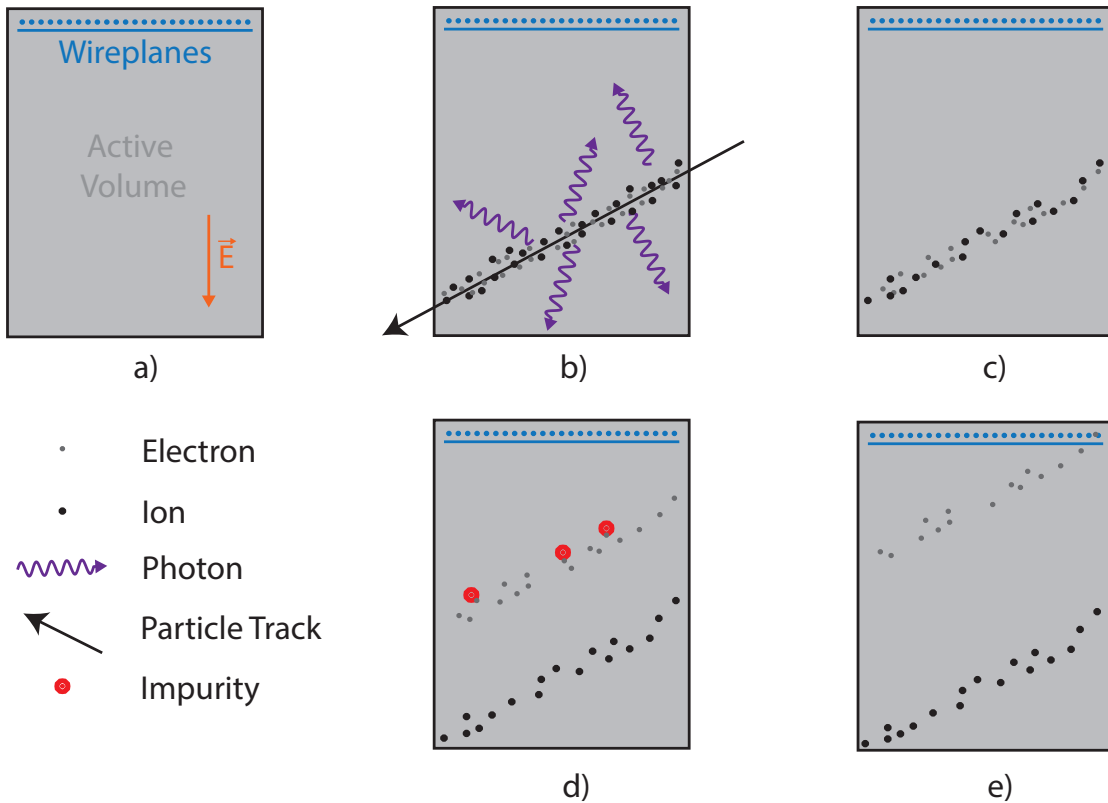
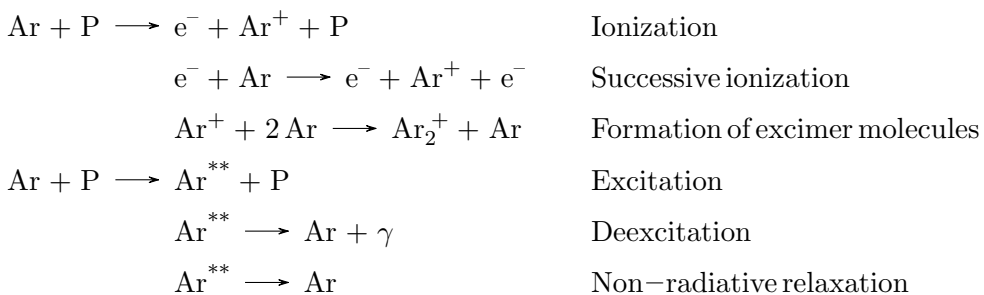


FIGURE 3.2: Illustration of different processes inside a TPC in order of time: a) description of sketch, b) charged particle passing through active volume inducing ionization and scintillation, c) recombination losses, d) drift through the detector and electron attachment to electronegative impurities, e) further drift towards wireplanes and subsequent readout.

an electron in the argon atom to a higher level, which will subsequently return back to its ground state via the emission of photons with characteristic energies or by collisions with other atoms producing heat (non radiative relaxation). A schematic summary of these two processes is given in the following reaction diagram, where P stand for the incident particle, Ar for the argon atom, Ar^+ for the argon ion, Ar^{**} for the excited argon atom and e^- for the electron.



The conversion efficiency of the absorbed energy into measurable ion-electron pair signals, lowered by the process of excitation, is given by the mean energy needed to create

an electron-ion pair W_i . The value can be expressed in terms of the mean energies for ionization E_i , excitation E_{ex} and sub excitation E_{se} , and the ratio between the number of excited and ionized atoms N_{ex}/N_i :

$$W_i = E_i + \frac{N_{ex}}{N_i} E_{ex} + E_{se}. \quad (3.1)$$

This relation is known as Platzman equation (see [32]). Experiments indicate a slightly higher mean ionization energy E_i than the expected band gap energy E_g of $E_i/E_g = 1.08$. The ratio between the number of excited and ionized atoms is experimentally determined to be $N_{ex}/N_i = 0.26$ for liquid argon and the mean excitation energy is measured to be $E_{ex} = 0.89E_g$. Using a so called gas model one can estimate the value for E_{se} to be $0.33E_g$. Combining these results leads to a theoretical value of $W_i = 23.452\text{ eV}$, which is in good agreement with the experimental value $23.6^{+0.5}_{-0.3}\text{ eV}$ [28]. Disregarding recombination effects this leads to a formation of approximately 9000 electron-ion pairs per centimetre for a minimum ionizing particle.

The energy needed to produce an ion-electron pair will fluctuate according to a Poissonian distribution with a variance $\delta = \sqrt{N_i}$, where N is the number of charge carriers produced, ultimately limiting the statistical energy resolution of the detector. An additional factor needs to be introduced because the formation of charge carriers is not independent of each other, violating the assumption of a Poissonian distribution: $\delta = \sqrt{F \cdot N_i}$. This factor is called Fano factor and for liquid argon $F = 0.107$ from [11]. Disregarding any additional fluctuations (electronic noise, drift, ...) and recombination leads to an energy resolution $R_{Statistical}$, defined as the FWHM (full width at half maximum) at a given energy:

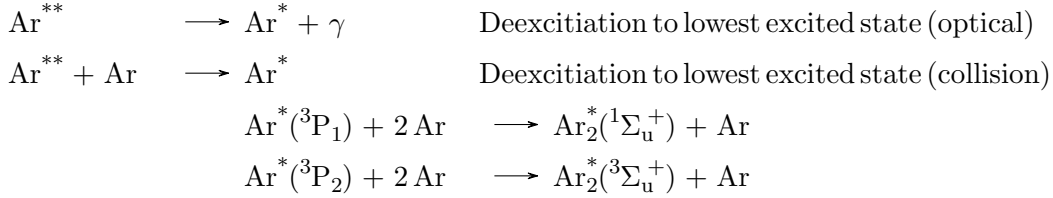
$$R_{Statistical} = \frac{FWHM}{E_0} = \frac{2.35W_i\sqrt{FN}}{W_iN} = 2.35\sqrt{\frac{F}{N}}. \quad (3.2)$$

For a minimum ionizing particle the statistical resolution limit is therefore fixed to $R_{Statistical,MIP} \approx 2.5\%$.

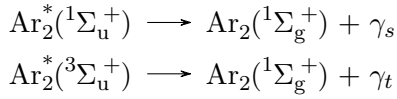
The deexcitation of liquid argon linked to the emission of a photon could be interpreted as scintillation, but the process is possible in the opposite direction too, absorbing the emitted photon again. This behaviour is known as radiation trapping, the characteristic photon is only observed in very low pressure gaseous argon (see [14]).

Therefore other processes are responsible for efficient scintillation in liquid argon. The main reaction is the following: Excited argon atoms Ar^{**} reach the lowest excited states Ar^* through collisions with other argon atoms or optical transitions [15]. These excited states can subsequently decay into the ground state of the argon atom, but as already mentioned above, the emitted photon will be absorbed by argon atoms preventing the photon to leave the liquid argon. But through collisions with neighbouring atoms the excited argon atoms Ar^* can form excited argon molecules, called excimers, which are only stable as an excited state. Due to the different possible lowest excited states, corresponding to different electron shell configurations (namely 3P_1 and 3P_2), two distinguishable excimer states can form. These states are formed within picoseconds after

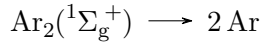
the ionization because of the high density of liquid argon [23], a detailed description of the formation and structure of argon excimers can be found in [30]. The formation of argon excimers is summarised in the following reaction diagram:



These two excimer states are singlet (${}^1\Sigma_u^+$) and (${}^3\Sigma_u^+$) triplet states. Both states decay to the excimer ground state via the emission of a deep ultraviolet photon:



Because the repulsive electric force of the two argon atoms in the excimer ground state is not any more compensated by the electric bounding which was present in the excited state, the excimer will separate into two isolated argon atoms:



The singlet decay represents the allowed decay channel with a lifetime τ_s of several nanoseconds whereas the triplet decay is a forbidden dipole transition. Only due to the mixture of the triplet state ${}^3\Sigma_u^+$ with the ${}^1\Pi_u$ states allows the triplet state to decay [21]. This small mixture is the reason of a relatively long lifetime τ_t of the order of microseconds. The emitted photons have very similar wavelengths of 126.6 nm for the singlet decay and 127.6 nm for the triplet decay and a width (FWHM) of about 10 nm [29]. Because of the large separation in time and the close emission peaks the two lifetimes are well measurable as seen in Figure 3.3. Because of the very short time needed for the formation of argon excimers and the subsequent decay after ionization, the detection of the emitted photons is well suited for the measurement of the absolute time when a particle interaction happened inside the detector.

If no electric field is present when a particle ionizes liquid argon, the produced electrons will thermalize and will be captured by positive argon excimers Ar_2^+ , forming an excited argon atom Ar^{**} and a Ar atom. This argon atom will subsequently decay following the scintillation process described in the previous section. The process is called recombination and results in the full conversion of the absorbed energy into scintillation apart from losses into non-radiative energy dissipation (heat).

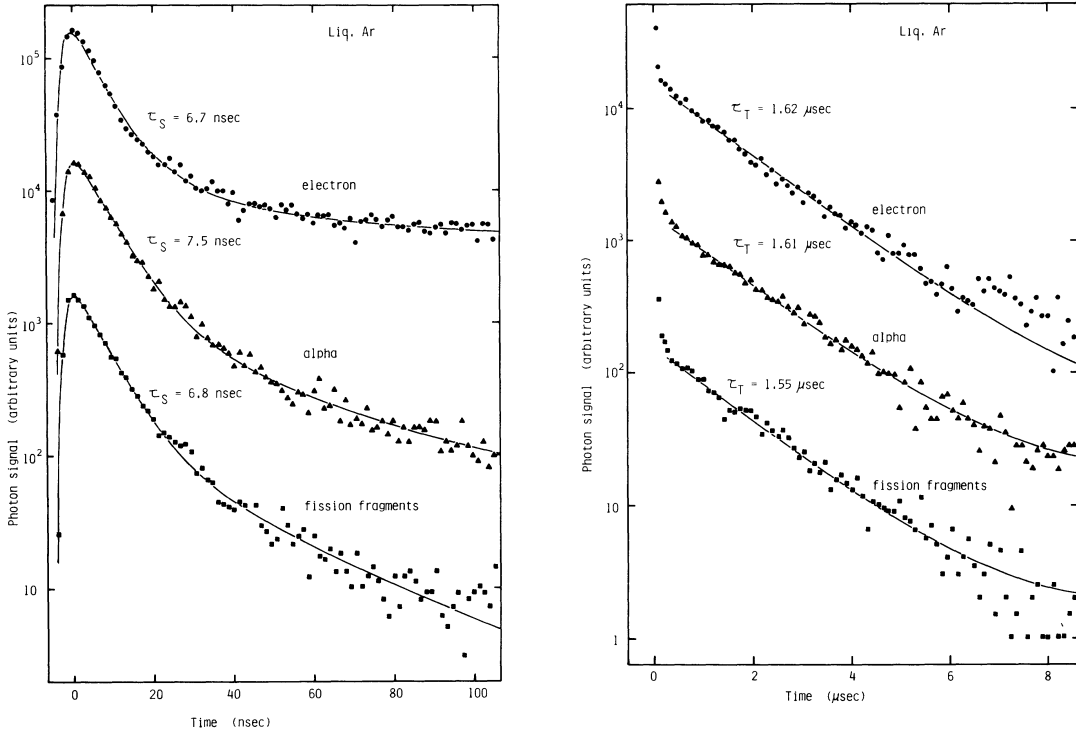


FIGURE 3.3: Plot of the time resolved scintillation intensity in the VUV-range for different ionizing particles (electrons α -particles and ions). Two different lifetimes (τ_S and τ_T) (singlet and triplet) are distinguishable in the two different time scales. From [17].

However, if an electric field is applied, the electrons and positively charged argon excimers will spatially separate, decreasing the recombination rate. Several models were developed to describe the recombination process under the presence of an electric field, but were only valid in certain field strengths regions, before the "box model" was introduced by Thomas and Imel [37]. Building up on the previous models, the box model assumes that the electron-ion pairs are uniformly distributed along a column of the primary ionizing particle track and that the electrons and ions are spatially separated by approximately 100 atomic spacings. Because the ion mobility is five orders of magnitude smaller than the electron mobility in liquid argon (see table 3.1), the model considers the ions to be stationary during the recombination process. The electron diffusion is as well neglected since the value is small in the considered timescales and the electric field is assumed to be uniform in space and time. Including these assumptions into a continuity equation considering recombination as a sink term leads to an exact solution of the problem:

$$\frac{Q}{Q_0} = \frac{1}{\xi} \ln(1 + \xi), \quad \xi = \frac{N_0 K_r}{4a^2 u_- E}. \quad (3.3)$$

where Q/Q_0 is the fraction of free charge after the recombination process and ξ is the parameter on which the model depends. The parameter is influenced by N_0 the number of electrons in the box, K_r the recombination rate constant, a the size of the box, u_- the electron mobility and E the electric field strength. The fraction of collected charge

will follow the relation $Q/Q_0 \propto E \ln(1 + 1/E)$, going to zero for $E = 0$ and to 1 for $E \rightarrow \infty$.

Figure 3.4 shows data points for the collected charge and light for a variable electric field as well as the theoretical expected curve for 0.976 MeV and 1.05 MeV electrons. These measurements clearly illustrate the relation between light yield and collected charge, since with increasing electric field strengths more electrons are prevented from recombination which would follow the scintillation process.

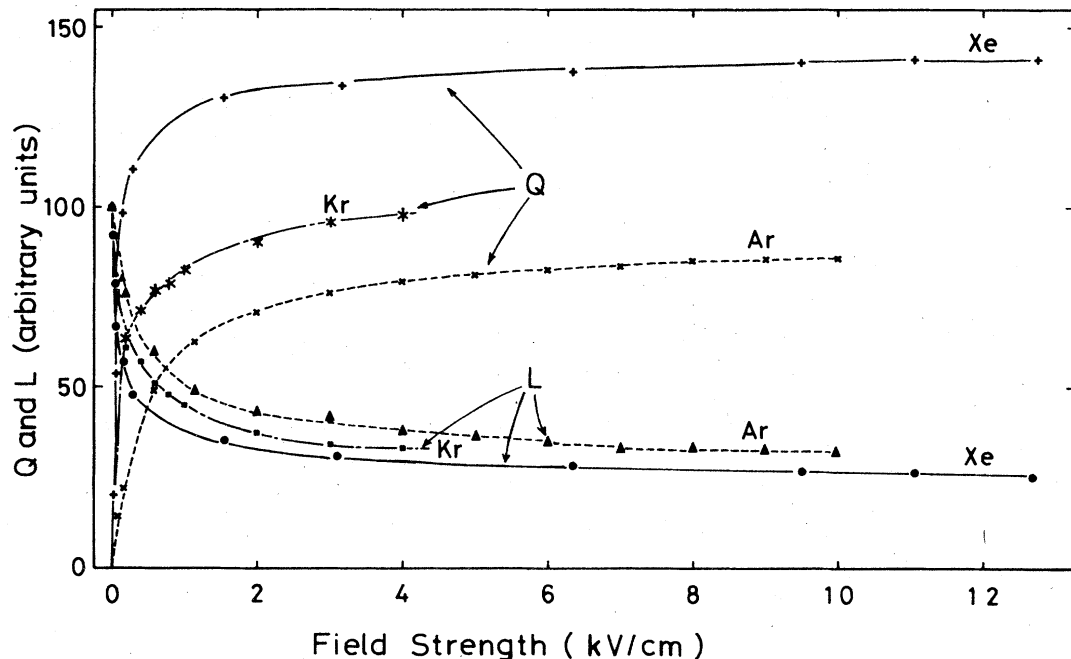


FIGURE 3.4: Light (L) and charge (Q) yield as a function of the applied field strength for argon, xenon and krypton. From [21].

The velocity of charged particles in an electric field is governed by the equation $\vec{v} = \mu \vec{E}$, where μ is the mobility of the particle and \vec{E} the electric field, the vector nature of this relation states that the charged particle will follow field lines. Therefore a well known electric field inside the detector is necessary to reconstruct the position of the charge produced inside the detector. For the same reason the drift velocity at a given electric field strength has to be known precisely.

Electrons are considered quasifree in liquid argon because of the high mobility of $\mu_e = 0.048 \text{ m}^2 \text{V}^{-1} \text{s}^{-1}$. The linear relation between drift velocity and electric field holds for low field strengths up to 100 V/cm, above this threshold a saturation of the drift velocity is observed which is generally accounted to the increase of the electron mean energy by the electric field (see [26] for a detailed discussion). The electric field strength in time projection chambers lies generally between hundreds of V/cm and several kV/cm, in Figure 3.5 the electron drift velocity in this region is plotted for different temperatures.

The experimental obtained results were fitted with a model of the form:

$$v_d(T, E) = (P_1(T - T_0) + 1)(P_3 E \ln(1 + \frac{P_4}{E}) + P_5 E^{P_6}) + P_2(T - T_0). \quad (3.4)$$

A global χ^2 -fit was used to obtain the parameters P_1 to P_6 with a fixed $T_0 = 90.371$ K. The numerical values and further details of the model are given in [41].

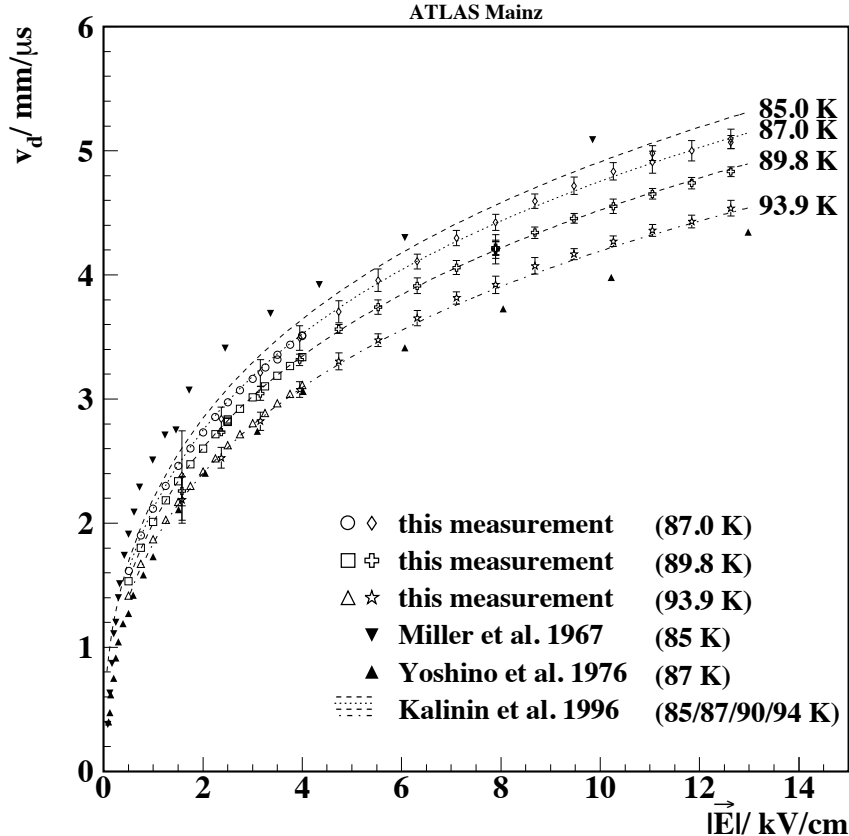


FIGURE 3.5: Drift velocity in liquid argon versus electric field strength for different temperatures [41].

Electrons drifting through pure liquid argon would allow for a direct measurement of the produced charge during the ionization process, but in reality impurities in the liquid argon are always present. Electronegative impurities, such as hydrogen and oxygen, will trap electrons and extract them from the signal generation process, if the impurity level is to high all produced electrons will be trapped. The capturing process can be described in terms of the number of free electrons

$$N(t) = N_0 e^{-t/\tau_e}. \quad (3.5)$$

where N_0 is the initially produced number of electrons, t is the drift time which is related to the drift distance over the velocity and τ_e the electron lifetime. The electron lifetime

τ_e is connected to the concentration of impurities n_i via the relation

$$\tau_e = \left(\sum k_i n_i \right)^{-1}. \quad (3.6)$$

Where k_i is the characteristic electron capture efficiency for the different impurities. Usually the impurity concentration is given in O₂ equivalent and a rule of thumb exists for the relation between O₂ equivalent impurity in ppb and the electron lifetime

$$\tau_e [\mu s] = \frac{300}{P_{O_2 equiv} [ppb]}. \quad (3.7)$$

3.3 Laser Calibration System

sec:laser) Opposite to electrons, argon ions have a several orders of magnitude lower mobility in liquid argon, resulting in a lower drift velocity of the order of 1 cm/s. This leads to an enhanced residence time of positive charge inside the detector and accumulation of positive ions inside the detector. This process called build up of space charge will alter the electric field such that a simple reconstruction, assuming a homogenous electric field, is not possible anymore. In Figure 3.6 (bottom) the electron drift path in a physical detector for two identical initial particle tracks in a homogeneous and distorted electric field is shown. For both cases the readout signal is depicted (top) as well, here the z-axis information of the physical detector is resolved in time and reconstructed assuming a homogenous drift with drift speed according to equation 3.4. This assumption introduces an erroneous reconstruction of the initial particle track, as can be seen by the comparison of the two trajectories in the readout plots. Because of the distorted field lines the reconstructed track is broader, the longer drift time implies a shift of the track and the combination of both effects distorts the initial particle track. The introduced field distortion approximated the accumulation of space charge at the cathode in the detector. The effect is pronounced in larger volumes because of the higher total charge accumulated leading to a stronger distortion of the electric field. A detailed discussion of the implications of the build up of space charge due to cosmic particles in ionization chambers can be found in [31].

A first simulation with an increasing space charge distribution according to [31] towards the cathode was performed in 2D for the MicroBooNE detector configuration [38]. The result of this study is shown in Figure 3.7, in the upper left corner a sketch of the TPC geometry (red) with the axis labels is shown. Also the chosen simulation plane (blue) with the different cross sections on it is depicted. The cathode is located at the right ($z = 2.5$ m) and the wireplane (anode) at the left ($z = 0$ m). The plot on the top right shows the assumed field charge distribution along the z -direction inside the detector, outside the charge distribution is assumed to be zero. On the lower left the vertical electric field distortion E_y relative to the desired horizontal electric field E_z is plotted for different vertical cross sections (parallel to the z-axis) inside the detector. Alongside

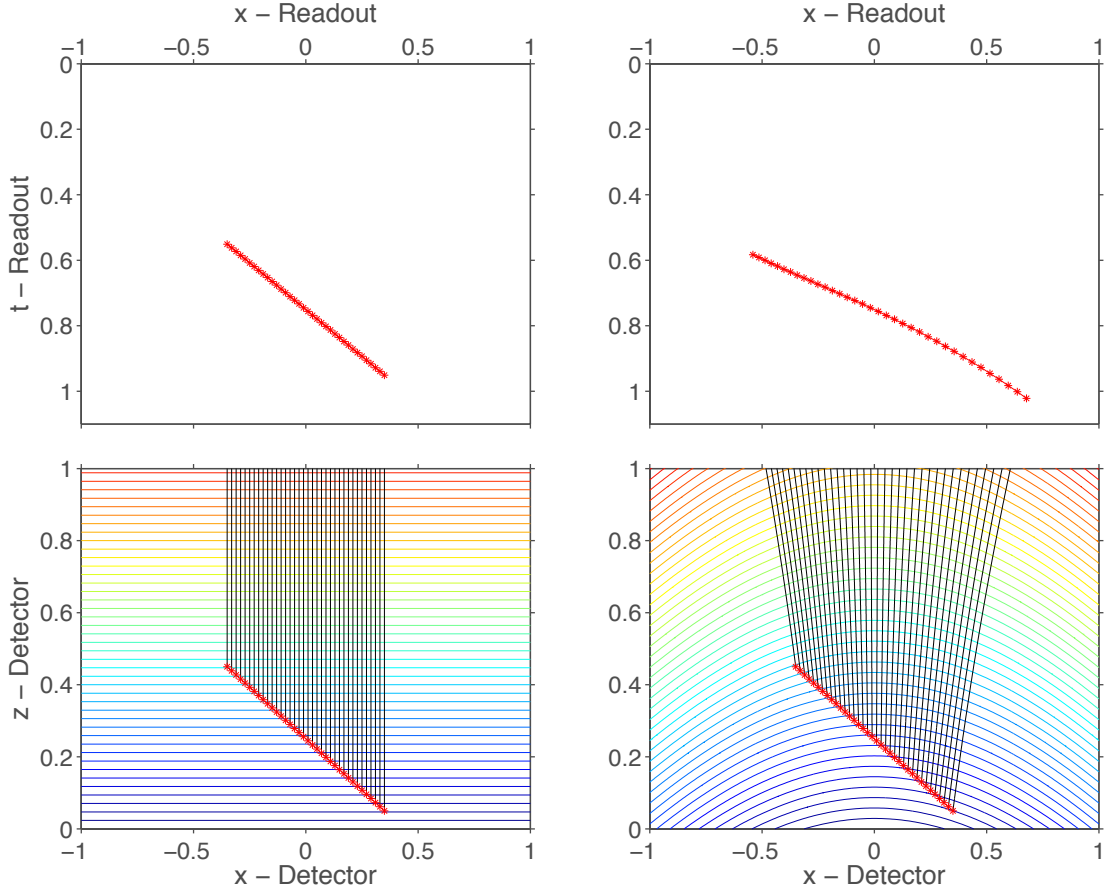


FIGURE 3.6: Illustration of the field distortion effect on track reconstruction. In the lower column a physical detector is depicted. Coloured lines represent the electric potential which implies a downward looking electric field. In the left picture a homogenous field is present whereas in the right a distortion is added. A possible particle interaction is introduced with red stars, black lines show the trajectory of the produced electrons. At $z = 1$ the signals are read out by an ideal wireplane. For each field configuration the corresponding reconstructed tracks are shown in the upper column.

the corresponding displacement of a track in the detector as a function of the distance from the anode is shown. The displacement ranges from less than 1 cm near the readout plane up to 10 cm close to the cathode.

The effect of space charge build up strongly affects a large detector if it is located at earth surface, because an enhanced rate of cosmic particles will constantly ionize the liquid argon. Therefore the field inhomogeneity will increase and the reconstruction of the interaction in the detector will be less precise.

A possibility to diminish the muon flux is shielding the detector against cosmic particles by movement to an underground site. Another possibility to account for the problem is the calibration of the drift field inside the detector, to reconstruct the field inhomogeneity and implement a spatial correction in a later step during the analysis of interaction events. With a calibration map not only space charge effects are resolved, but also possible temperature variations and relative misalignment of the support structure affecting the drifting charge are measured. The calibration is obtained by the introduction of a

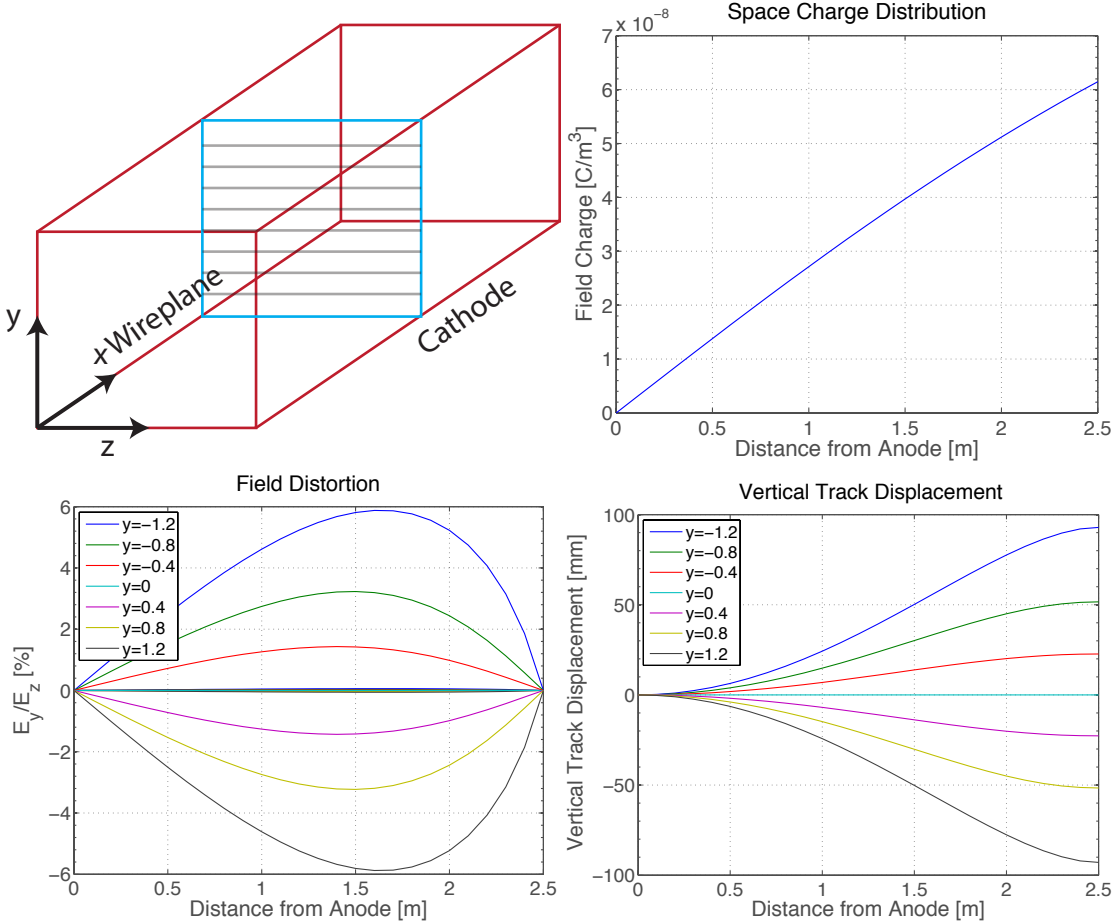


FIGURE 3.7: A simulation of the space charge effect on drifting charge in MicroBooNE. In the upper left a sketch of the TPC and labelling is shown. For the simulation the space charge according to the plot in the upper right corner is assumed. In the lower column the simulated ratio of E_y/E_z vs. the distance (left) from the anode and the resulting vertical displacement vs the distance from the anode (right) is plotted for different vertical cross sections. Plots adapted from [38].

straight laser beam into the detector. Conducting a full scan of the detector will result in a set of tracks in the liquid argon time projection chamber, which can be used to obtain a correction map for the subsequent event analysis. So far several laser calibration systems have been implemented into gas time projection chambers [22], [33] and [27], but no realisation of such a system has been employed on a LAr TPC.

The ionization potential of gaseous argon is approximately 15 eV [40] corresponding to a photon wavelength of 83 nm. Laser systems emitting light in this wavelength region are not commercially available, however argon can be ionised by the simultaneous absorption of multiple photons of lower energy (higher wavelength). Two-photon absorption can excite the argon atom from the ground state into an excited state, from where an additional photon can further lift the atom above the ionization energy. In Figure 3.8 the energy levels of interest for gaseous (left) and liquid (right) argon are plotted, in liquid argon the energy levels are reduced by polarisation effects as well as broadened. Also plotted is the photon energy of a commercially available UV-laser system with

wavelength 266 nm ($E_\gamma = 4.6 \text{ eV}$). The low cross-section for two photon absorption and the very short lifetime of the excited state imply a low total cross-section for the 2 plus 1 photon absorption. A detailed discussion of the relevant processes can be found in [7], the feasibility of a 266 nm Nd:YAG laser system for liquid argon ionization has been shown in [36] and was used for purity measurements in [12].

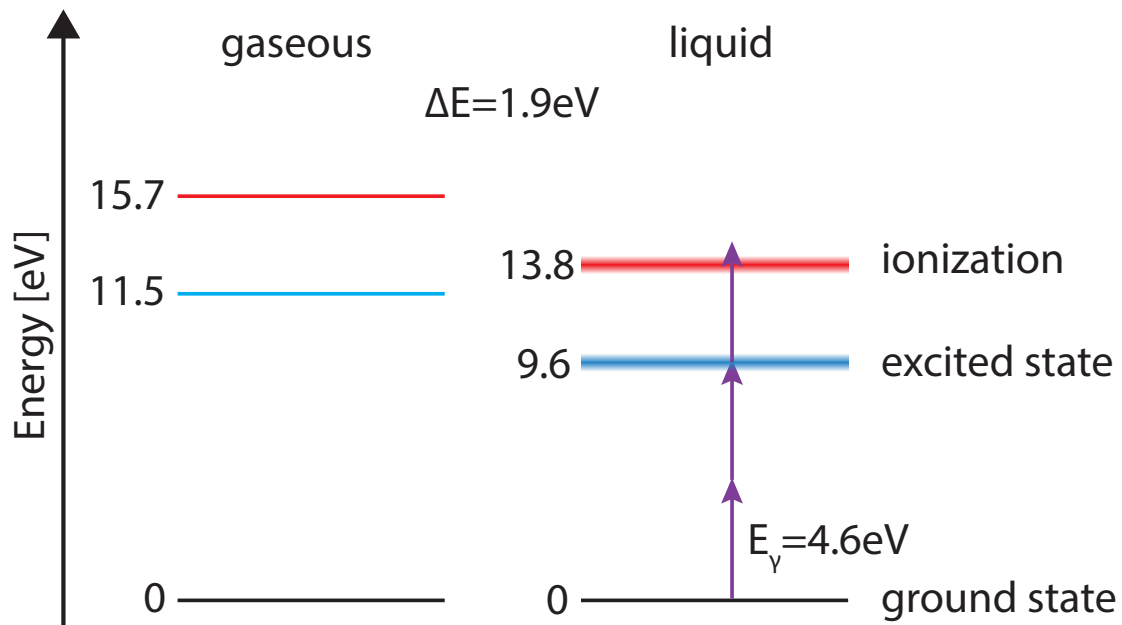


FIGURE 3.8: Energy levels of gaseous and liquid argon relevant for UV-laser absorption.
Plot adapted from [7].

Chapter 4

Experimental Setup

A calibration system including an UV-laser, an optical table and a motorised and position encoded feedthrough was designed and tested. The design aimed at the integration of the system into MicroBooNE and the presented setup is the first step towards daily operation in the experiment. The test of the laser calibration system was conducted in the so called medium Argontube cryostat, which was previously used for liquid argon experiments. In the following I will describe the individual parts of the experimental setup in detail.

4.1 Cryogenic Environment

The enclosure system consists of two stainless-steel vessels, the inner vessel contains all parts of the detector and is vacuum tight to ambient air. The outer vessel is used as a bath for cooling the inner vessel to liquid argon temperatures. To achieve the required purity of liquid argon for the electrons to drift, a ultra pure environment is introduced around the detector. Before the liquid argon is filled into the cryostat, the vessel is evacuated. This procedure removes the residual air as well as impurities on the surfaces inside the vessel. The vessel was usually evacuated over several days.

The inner vessel is 125 cm high and has a diameter of 50 cm corresponding to a volume of about 2001. Vacuum tightness between the top flange and the inner vessel is guaranteed by an indium sealing which is imbedded in a groove on top of the vessel. Several smaller flanges are positioned on the top flange, here the sealing is realised with a copper gasket and knife-edge flange (ConFlat or CF). All parts of the detector were cleaned with alcohol before installation. A diagram of the full piping setup is shown in Figure 4.1. The vacuum generation was realised in two stages connected in series: A rough vacuum was generated by a rotary vane pump (P1) and high vacuum was achieved by a roots pump (P2) which was connected to the vessel via a pipe with 100 mm inner diameter. At the end of the pipe a high vacuum gate valve was installed, which was closed after

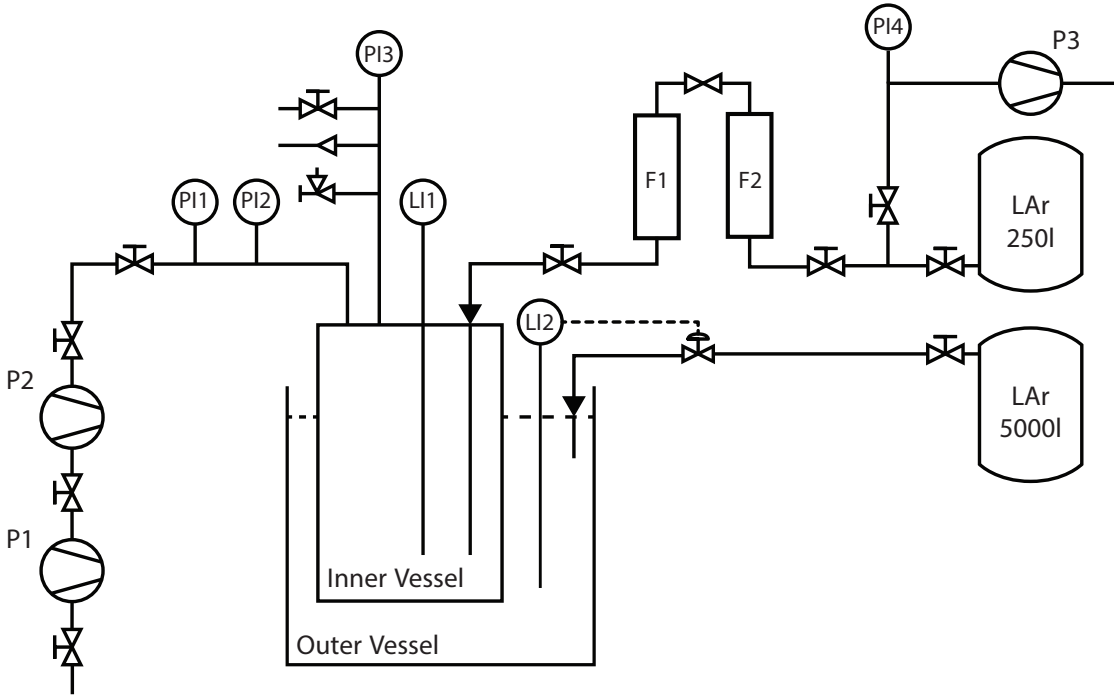


FIGURE 4.1: Piping and instrumentation diagram of the experimental setup. Left of the vessels the vacuum part is drawn and on the right the liquid argon piping and handling is drawn. Here P stand for vacuum pump, PI for pressure indicator, LI for level indicator, F for filter and LAr for liquid argon.

sufficient pumping. The vacuum was monitored by a Pirani gauge (PI1) in the region 10 to 1×10^{-3} mbar and a Penning gauge (P2) below 1×10^{-3} mbar, an additional pressure gauge (PI3) was installed to monitor the overpressure in the vessel. This overpressure was maintained to prevent ambient air to flow into the cryostat during runtime operation with liquid argon. A relief valve (opening at 300 mbar overpressure) was installed for safety reasons.

After sufficient pumping the liquid argon was filled into the vessel, because liquid argon has a temperature of 89.8 K cryogenic equipment is needed. The outer vessel which acts as a cooling bath is filled with factory grade liquid argon, to counteract buoyancy forces the inner vessel is fixed to the outer vessel. As soon as the outer vessel has reached a threshold level, a feedback loop (LI2) is activated. This loop controls the valve of the liquid argon support line and refills the outer vessel if the level drops below a preset value due to constant evaporation. The liquid argon is supplied from a 5000l tank. The inner vessel is filled with liquid argon over a separate filling line connected to a 250l pressurised dewar. Two filters are introduced to remove impurities from the factory grade liquid argon, filter F1 is a Hydrosorb filter removing hydrogen and F2 is a Oxisorb filter removing oxygen. Both filter types are commercially available from Messer¹. The filling line is evacuated (with PI3), before liquid argon is introduced, to prevent residual air to enter the filters and saturating them. Because the filters introduce high resistance in the filling line, an overpressure of 6 bar is built up to reduce the filling time. As

¹www.messergroup.com.

soon as overpressure is measured in the inner vessel a vent is opened to relief the argon gas which is evaporating at the warm surfaces in the inner vessel. Subsequent cooling of these surfaces will end in condensed argon present in the inner vessel. The level of the liquid argon is monitored with a level meter (LI1). When the desired inner level is reached the vent is closed and the liquid argon supply line is closed. An unidirectional valve is installed to prevent a build up of pressure inside the inner vessel because of constant heat input from the top flange. After the filling process the two filters contain residual liquid argon, which will evaporate when the filters warm up, therefore only the valve after the filters is closed to stop the filling process and the overpressure in the supply dewar is reduced. In this configuration the argon gas can circulate back into the dewar. When the filters reach room temperature the valves can be closed and the dewar can be removed.

4.2 Time Projection Chamber

The TPC consists of a cathode on which a high voltage is applied, a cascade of resistors connect the field shaping rings and the wireplanes. Here an array of thin wires is spanned to cover the full $20 \times 20 \text{ cm}^2$ readout plane. Two such planes lie, separated by a small gap, above each other. These wires are each connected to the data acquisition system (DAQ).

In Figure 4.2 the detector electric layout is pictured. An aluminium disk of diameter 90 mm and a thickness of 3 mm on which a negative voltage (-HV) is applied acts as the cathode. The high voltage is introduced into the vessel by a feedthrough designed and manufactured in-house [20]. A $20 \text{ M}\Omega$ resistor (R_1) connects the cathode with the first field shaping ring, with an outer diameter of 90 mm and an inner diameter of 72 mm and 3 mm thickness. In total seven field shaping rings of the same shape follow. An inter-ring distance of 23 mm is realised with three spacers per plane, held together by a threaded bar, both made out of nylon. Again the rings are connected via $20 \text{ M}\Omega$ carbon resistors (R_2 to R_9) in between the rings. The edges of the rings have a curvature to prevent high electric field strengths. The last ring is connected to the lower surface of the PCB of the induction wire plane again via a resistor. The field just in front of the induction wireplane is kept at the exact same value as the field inside the detector via the adjustment of the resistor R_{10} connected to the upper copper plane of the induction PCB. This plane and the wires are kept at a voltage U_{ind} controlled from outside the cryostat. The collection plane voltage U_{col} , located 3 mm above the induction plane, could be controlled separately as well. A mechanism was developed for shortening deliberately the rings 3 and 4 (counted from the cathode), enabling the introduction of a controlled known field inhomogeneity.

Two wireplanes at the anode of the detector are used for the readout of the TPC. The voltages of the wires are controlled from outside in a way that the first wireplane is transparent to drifting electrons. On each wireplane 64 separate wire channels are

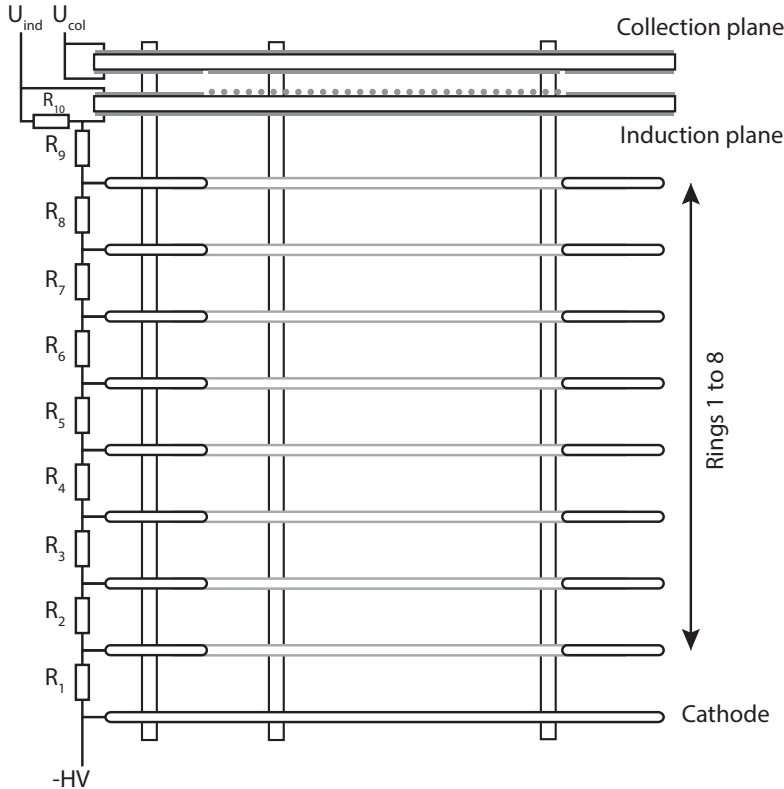


FIGURE 4.2: Schematic drawing of the detector including the cathode, field shaping rings and wireplanes. Also shown is the resistor cascade and its electric connections.

installed with an inter-wire distance of 2 mm. Each wire is connected to the controlled voltage (U_{col} or U_{ind}) over a $2.2\text{ M}\Omega$ SMD resistor on one side, and over a decoupling capacitor of 1nF to the readout. A perpendicular orientation of the two wireplanes to each other is realised.

The typical electrical ionization signal is of the order of thousands of electrons when it reaches the wire. Such a small signal can not be digitalised efficiently, therefore cryogenic charge preamplifiers are put as close as possible to the wires, reducing possible noise introduced by cables, to increase of the signal to noise ratio. The data acquisition setup is shown in Figure 4.3. In the presented setup application specific integrated circuits (ASICs), developed at Brookhaven National Laboratory [10] especially for low temperatures, were used as the first amplification stage. These ICs have a configurable gain and peaking time for each channel, usually a gain of 25 mV/fC and peaking time of $1\text{ }\mu\text{s}$ was set. One IC houses 16 individual 5th order amplification stages, four chips were used to readout 32 induction and 32 collection channels. The four IC were mounted on two PCB which were directly plugged into the wire support PCB to ensure short signal paths. A further advantage of these chips is the online access to the amplification and shaping factors, these can be adjusted to the needs via a serial link and the chips can be daisy chained among each other, reducing wiring. In MicroBooNE the same ASICs will be used for signal amplification.

After amplification the signals were fed to a custom built feedthrough with two teflon

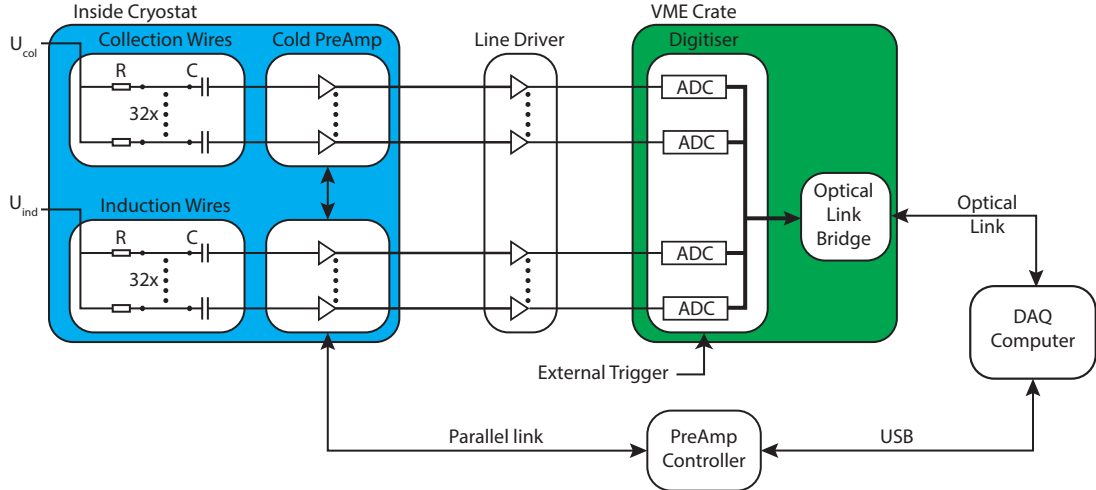


FIGURE 4.3: A schematic diagram of the data acquisition system from the signal formation on the induction and collection wires and cold amplification (in blue) via a line driver to the digitalisation (in green) and communication to the computer.

ribbon cables, each channel is interleaved between two ground lines to counteract pickup noise and crosstalk. On the warm side of the feedthrough a line driving stage is employed for impedance matching with the analog-to-digital converter. After this stage each channel is fed to the digitiser boards via separate MCX coaxial cables. Digitisation is realised by high speed 14bit analog-to-digital converters, one board (CAEN V1724) houses 8 channels. To digitalised all 64 channels, 8 boards are brought together in one VME crate, which is responsible for the communication among the boards. These boards have a adjustable sampling rate and use a ring buffer to store data. The sampling rate (typically 30 ns) and the number of pre- and post-trigger samples was adjusted to the needs of the specific measurement, in this study the relevant parameter is the drift time of the electrons in the detector. It defines the minimal time needed to resolve the full chamber in the recorded number of samples. Acquired data is send to a computer via an optical link by a controller board (V1728). On the computer the captured event can be displayed and stored. The responsible software was developed for previous liquid argon TPC experiments and was modified to the needs of this experiment. Only 8 digitiser board were available, this reduces the number of readout channels to totally 64 (32 in induction mode and 32 in collection mode).

The described readout setup is constantly filling the ring buffer included in the digitiser boards, but only when an external trigger signal is generated the data present in the ring buffer is sent to the DAQ computer. Triggering the readout was realised in two different ways, when recording laser events the signal of a photodiode (described in the following section) was used as a trigger input. For recording cosmic events, signals of up to four wires were split before the digitisation and additionally fed to an oscilloscope, which was used to employ a trigger pattern (single wire, single events, coincidence pattern). The trigger output of the oscilloscope was then fed back to the digitiser boards as an alternative trigger. Further improvement of the trigger pattern was achieved by using

the majority output mode of the CAEN V1724 digitisers. This mode outputs an analog level in steps of 0.125V for each input channel on which the input voltage lies above an individual channel threshold. Monitoring this output channel instead of single wires allows for an more efficient triggering because of the higher number of channels included for detecting events. The configuration of the majority mode was implemented into the digitiser control software especially for this test.

4.3 Laser Calibration System

In Section 3.3 the principle idea behind the laser calibration system is illustrated. A UV-laser is used as the primary light source, the energy of the beam can be adjusted and is then directed into the cryostat, where a steerable mirror is installed such that the volume of the detector can be scanned.

A Nd:YAG laser (Surelite I-10) from Continuum, Inc. emitting light at a wavelength of 1024 nm is used as the primary light source. Inside the laser head nonlinear crystals are installed in the beam line for frequency doubling and summing, resulting in a wavelength of 266 nm needed for ionization of liquid argon. For this wavelength the company specifies a output energy of 60 mJ for each 4 to 6 ns long pulse and a horizontal polarisation. The maximal repetition rate is 10 Hz; the beam has a divergence of 0.5 mrad. The laser can be controlled via a RS232 interface and by manual triggering.

An optical table, see Figure 4.4 for a overview of the setup, was developed to introduce the necessary parts in a stable and compact environment. For the optical table to be compatible with the MicroBooNE experiment only minor changes are necessary. With regard to the application of the optical table on MicroBooNE, the parts were chosen to be accessible remotely where necessary. The emitted laser beam contains not only ultraviolet light but also all other harmonics generated in the crystal and the primary light of 1024 nm. Dichroic Mirrors optimised to reflect only wavelengths in the UV region are used to filter higher wavelengths out. To absorb the transmitted wavelength behind the mirrors glass-ceramic plates are installed. The beam leaving the laser head is reflected by the first 45°-mirror into an attenuator. For optical adjustment and verification of the non-visible UV-beam a green alignment laser is placed behind this mirror and adjusted such that its path is coincident with the UV-laser beam. In the attenuator² a turnable $\lambda/2$ -plate enables to rotate the orientation of the laser beam polarisation. Behind this two parallel plates are installed such that the angle of the incident beam matches the Brewster Angle of the reflector. Modulating the polarisation of the beam allows to adjust the energy of the reflected beam. After the attenuator an aperture is put in the optical path of the beam, to control the beam diameter. The last part in the beam line is a remotely controllable mirror Zaber T-OMG. which directs the beam to the laser feedthrough on the cryostat. A photodiode³, which is sensitive in the ultraviolet region

²Altechna Wattpilot.

³Thorlabs DET10A/M.

detects the scattered light when a laser pulse was fired, the signal is then used as a trigger for data taking. For level matching of the photodiode signal a discriminator with TTL and NIM output was designed and fitted in a NIM crate. Both the UV-laser head and the optical table are mounted on a 15 mm thick aluminium plate.

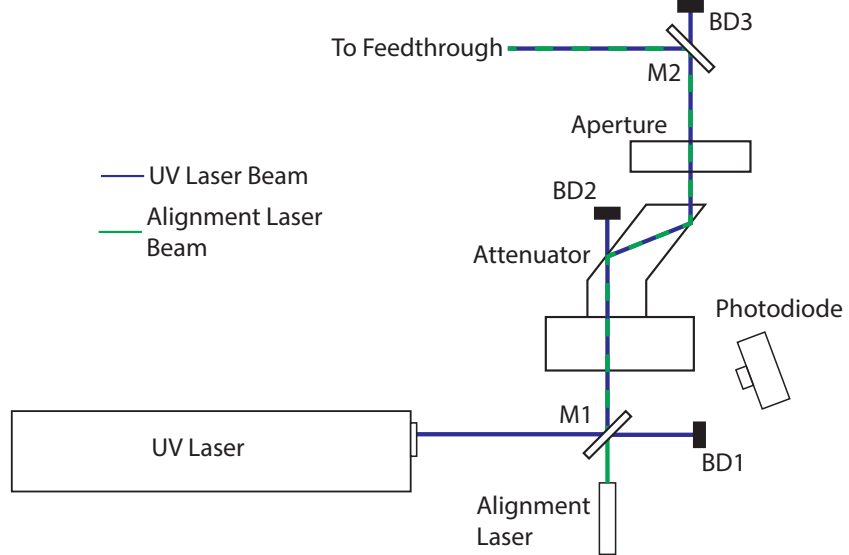


FIGURE 4.4: A schematic drawing (not to scale) of the components used for laser beam configuration. Into the UV-laser path an alignment laser path is introduced at the first dichroic mirror (M1), such that the paths overlap. In the attenuator the UV-laser beam energy can be adjusted to the desired level, the diameter of the beam is controlled by an aperture. A motorised mirror (M2) deflects the mirror into the direction of the feedthrough. Behind all mirrors beam dumps (BD) are installed to absorb the non-reflected laser light.

One of the main challenges of the laser calibration system for MicroBooNE is the introduction of a steerable laser beam into the detector. The approach developed and tested in this experiment is build upon the experience from previous experiments in our institute. Earlier an evacuated quartz-glass [7] was utilised to introduce a laser beam into liquid argon, however this beam had a fixed path through the detector. For the purpose of scanning the full detector a fully steerable cold mirror is needed. This goal is achieved by introducing a fully horizontally rotatable support structure for the cold mirror. A rack and pinion construction, where the mirror is mounted on the frontside of a half gear (pinion) provides the necessary freedom for the vertical movement.

A fully rotatable vacuum tight feedthrough was developed by the in-house mechanical workshop. It acts as a platform for the support structure of the mirror, a vacuum tight bellow on which the rod for linear movement is attached and an inner feedthrough which holds the quartz glass in the centre of the rotational movement. A first prototype of this setup was fully developed and machined by our mechanical workshop, it was not motorised nor equipped with position encoding and acted as a proof-of-concept prototype. In a second stage the movement was motorised: The rotational feedthrough was replaced by a commercial motorised differentially pumped feedthrough from Thermionics (RNN Series). This rotational feedthrough has three U-shaped ceramic seals which enclose

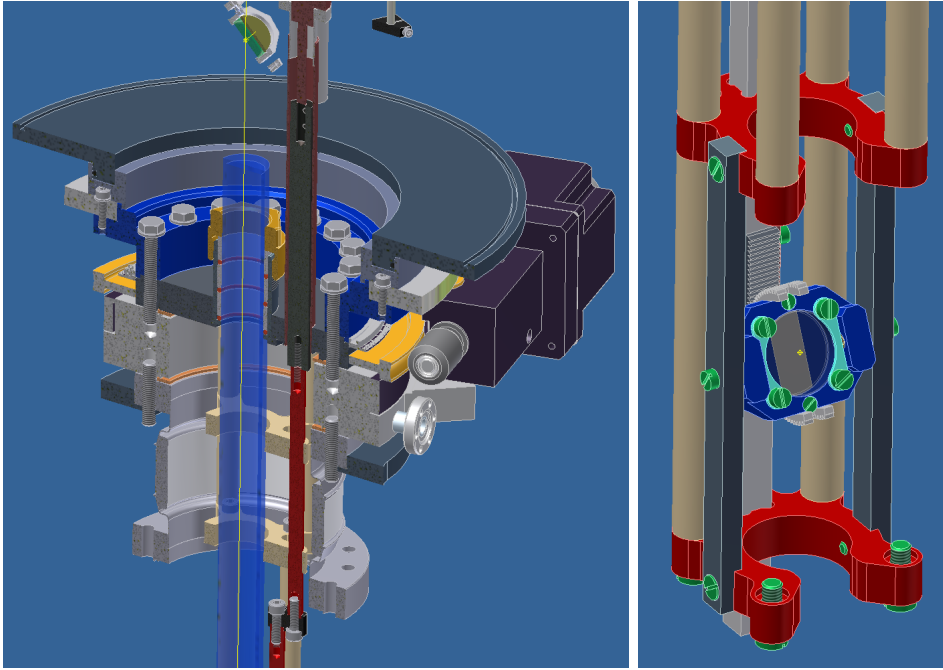


FIGURE 4.5: On the left a CAD drawing of the full setup feedthrough is shown. On the right the cold mirror including the support structure is depicted.

two gaps that can be evacuated. This design is foreseen for high vacuum applications, since the differentially pumped seals will close preferentially in one direction. However in this test, an opposite pressure difference is present when the liquid argon is inside the vessel. To minimise the leakage of ambient air into the inner vessel, the inner gap was constantly pumped with a rotary vane pump. From the same company a motorised precision linear feedthrough (FLMR) was installed. Furthermore the support structure was replaced by the final design fabricated out of polyamide-imide (Duratron T4301 PAI), which has a very low outgassing rate, low thermal expansion coefficient and is certified for operation at 87 K. To minimise the probability of discharges due to the close location of the feedthrough to the field cages in MicroBooNE, no conductive parts were used in the support structure. The support structure will have a total length of 2.5 m in MicroBooNE, in this test the length was reduced to 0.8 m because of the cryostats dimensional limits.

In a third and final stage both motors of the previous setup were equipped with high precision position encoders from Heidenhain. The precision of the encoders is chosen such that a position accuracy of 2 mm for the laser beam spot over 10 m distance is achieved. Both encoders rely on photoelectric reading of a measuring standard. An external interface box (EIB741) controls the encoders and is configured in a way that on a trigger signal (from the photodiode) the position reading is stored. Over an ethernet connection the DAQ computer can access the position data, and combine the data with the wire data. The same computer is also used for steering the two motors via a motor driver system (over a RS232 interface), alternatively a hand held terminal can control the motors independently. In Figure 4.6 a diagram of the motor controlling components

and their connections can be found. Software routines for controlling the motors and implementing the storage of the position data into the existing framework were developed for this test. This framework will be expanded and finalised for the use in MicroBooNE. In Figure 4.7 a sketch of the cold mirror position from a side and top view relative to the

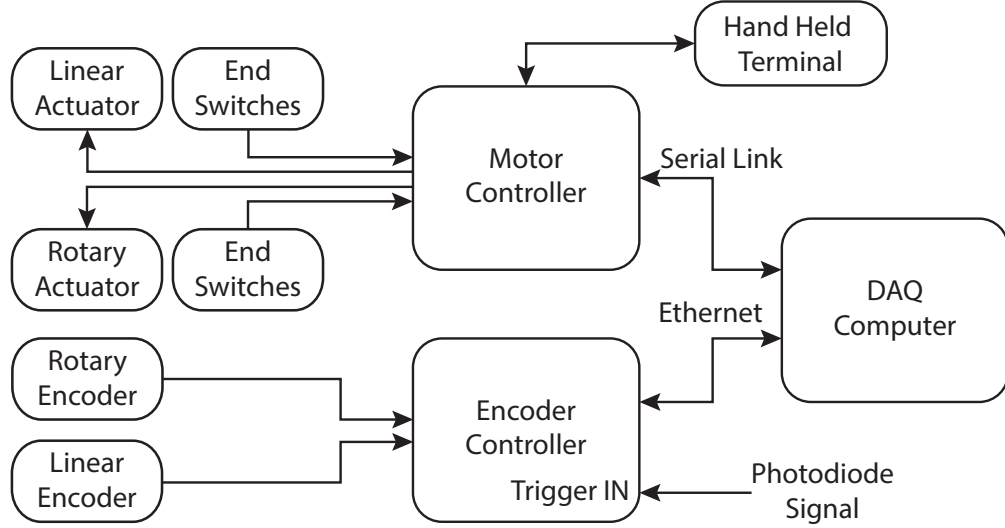


FIGURE 4.6: A schematic of the motor and encoder control system. The motor controller is connected to the linear and rotary motors and corresponding end switches. The movement can be managed by the DAQ computer or a hand held terminal. The position of the two motors is monitored by encoders connected to the encoder controller and stored if a trigger from the photodiode is present.

TPC is shown, also indicated is the laser path inside the TPC. The two angles $\varphi_{vertical}$ and $\varphi_{horizontal}$ as indicated in the Figure are used in the following to characterise the laser path.

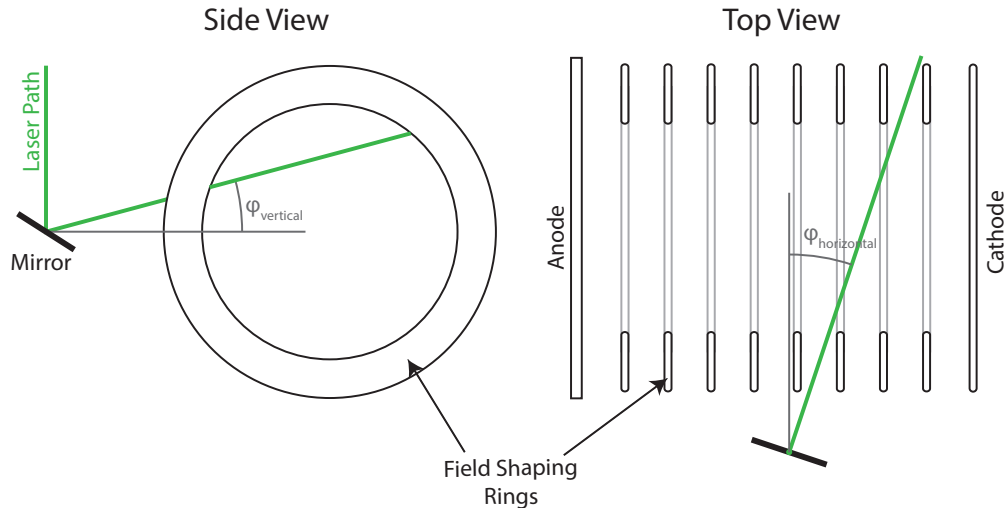


FIGURE 4.7: A sketch of the laser path in the TPC indicating the two angles used to characterise the laser path in the TPC.

Chapter 5

Experimental Results

Three measurement campaigns were performed, in a first run, all systems for a successful operation of the LAr TPC were tested. In a second step the laser system feedthrough was installed and first beams were introduced into the detector. The fully functional laser calibration system was operated and tested in a final run. Additionally measurements of the electron drift speed and argon purity which are not directly linked to the laser calibration system are discussed. An overview of the conducted measurement is given in Table 5.1.

Run	Start Date	End Date	Motivation	Recorded Data
1	25.3.2013	29.3.2013	TPC test	10000 cosmic events
2	13.5.2013	16.5.2013	Prototype feedthrough test	500 laser tracks
3	9.9.2013	14.9.2013	Full system test	2000 laser tracks
			Purity measurement	10000 cosmic events
			Drift speed measurement	1500 laser on cathode

TABLE 5.1: Overview of the measurement campaigns.

5.1 Test of the Time Projection Chamber

The motivation behind this first test is the establishment of an operational system for the further tests, as well as the familiarisation with all the subsystems. Because of the stepwise approach in which the complexity of the deployed subsystems is incrementally increased, possible errors can be identified more easily. For this reason the vacuum and cryogenic system and the TPC were tested without laser calibration system. The first goal to achieve was vacuum tightness of the inner vessel and a low leak rate. For these tests a helium leak detector was used, the leak rate was found to be 1.8×10^{-8} mbar · l /s. After pumping over three days the pressure in the vessel had reached a level of

2.3×10^{-5} mbar. Cooling the vessel to liquid argon temperatures contracts the full system and, if improperly installed, seals will cause leaks (due to different thermal expansion coefficients) which were not present under warm conditions. The cooling and filling of the inner and outer vessel took approximately 8 hours. The system was allowed to fully enter thermal equilibrium after filling by omitting any manipulations in the following hours.

The detector was taken into operation by ramping up the cathode voltage to 23 kV and applying bias voltages on the wireplanes ($U_{ind} = 0$ V, $U_{col} = 500$ V). The field inside the detector was set to 0.34 kV/cm. In this test, cryogenic pre-amplifiers were not yet installed, instead amplification was realised by a stage just after the signal feedthrough in place of the line drivers in Figure 4.3. Triggering on a single wire allowed to record muon tracks and other events. For further improvement of the triggering efficiency the majority mode triggering as described in section 4.2 was applied.

Wire signals for induction and collection of a muon track are shown in Figure 5.1. In Figure 5.2 and 5.3 recorded events are displayed, on the x-axis the sampling time, which translates into a drift distance when the drift speed is known, is shown. The y-axis indicates the channel number of the recorded event. The colour scale indicates the voltage amplitude of the recorded single wire. In the lower part induction signals and on top collection signals are shown.

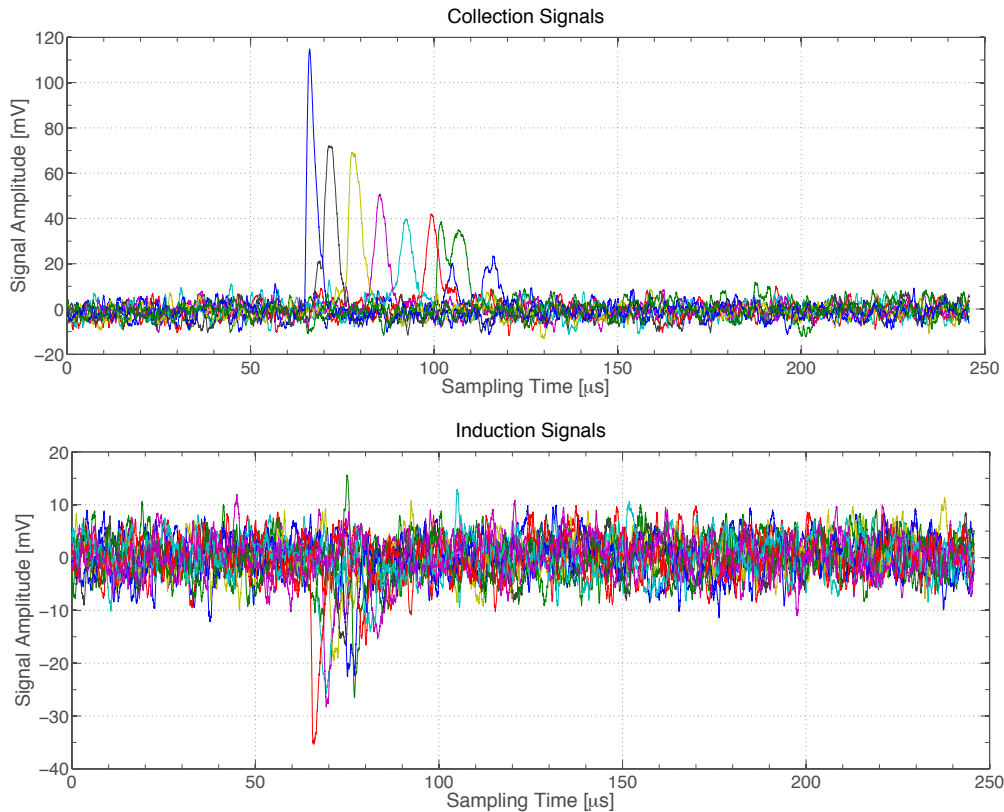


FIGURE 5.1: Typical collection (top) and induction (bottom) signals of the two wire planes, selected from event 53 in run 11.

Muon tracks were recorded over three days (approximately 10000 events), the purity of the argon did decrease because parts in the gaseous phase of the detector constantly evaporate impurities. The impurity level affected the recorded signal strength, which is visible in the observed length of inclined tracks. The observable track length of muons entering close to the wireplane and leaving the detector close to the cathode is reduced if more impurities are present, since the electrons produced close to the cathode have to travel longer distances. A higher impurity concentration will shorten the observable track length. After three days of operation the liquid argon level dropped below the field shaping rings and the run was stopped to prevent arcing on the field shaping rings in argon gas. This test successfully showed that the vacuum, cryogenic, detector and DAQ work properly and set out the conditions for further experimental runs.

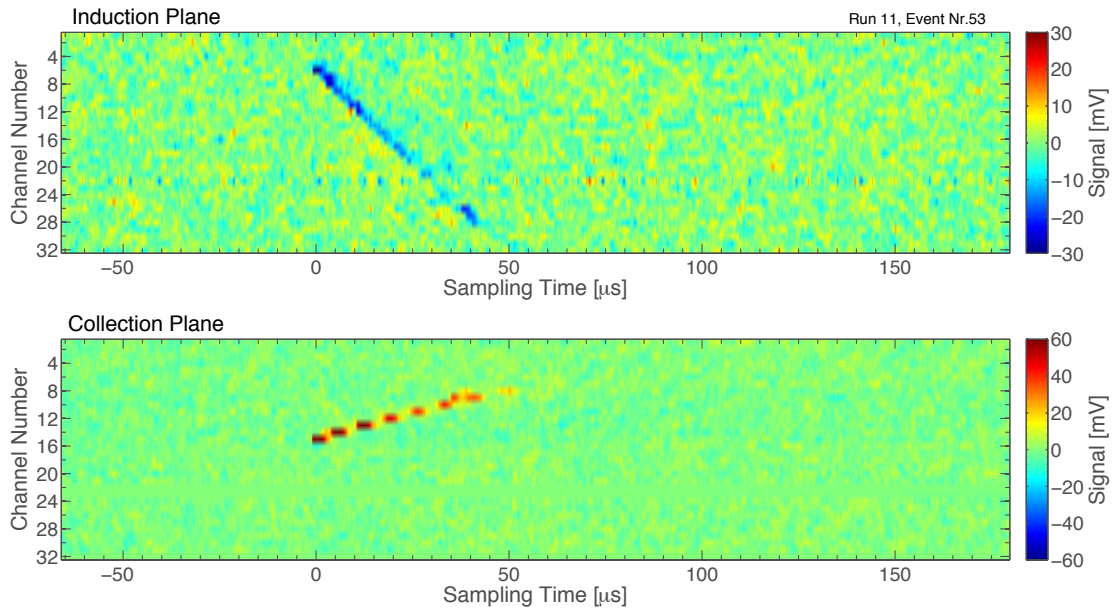


FIGURE 5.2: A recorded muon track with majority mode triggering.

5.2 Test of the Laser Feedthrough

The next step towards a full test of the laser calibration system was the integration of the laser beam and the introduction of the beam into the detector by a feedthrough. The already assembled and operational laser table was used to provide the UV laser beam. A first prototype feedthrough came to use, which was not motorised nor encoded. Rough measurements of the horizontal position were performed with indicators on the rotary feedthrough, a mechanical lock was used to hold the vertically movable bellow feedthrough in place. The movement of the feedthrough was done by hand. The filling procedure was identical to the first test, the leak rate and the achieved vacuum pressure did not deviate significantly from the previous values. The laser beam alignment between the (warm) mirror on top of the feedthrough and the steerable (cold)

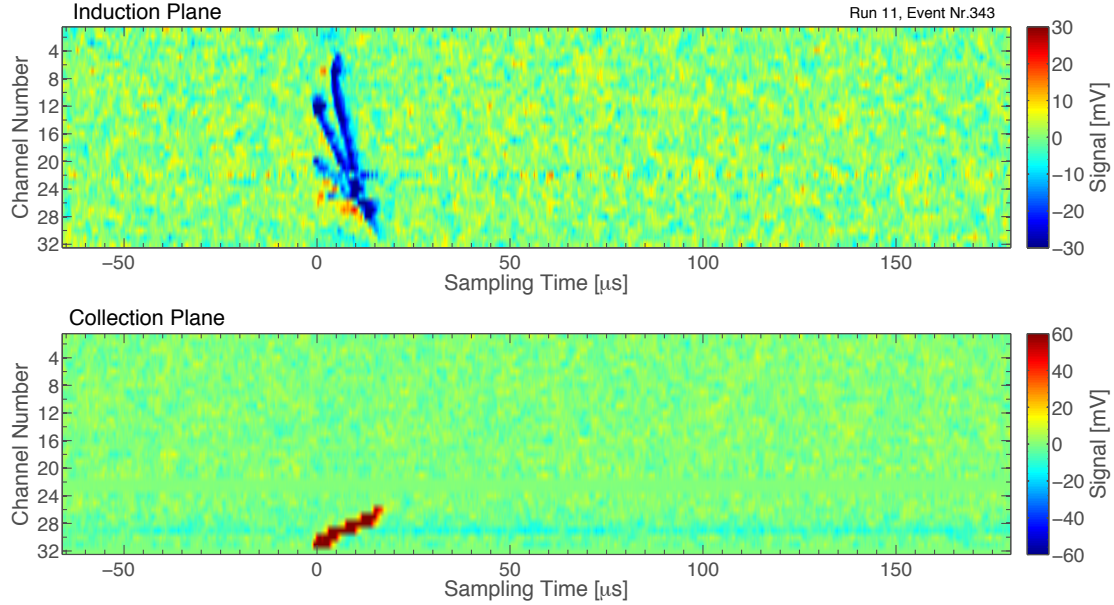


FIGURE 5.3: An electromagnetic shower recorded with majority mode triggering.

mirror in the cryostat was anticipated to be difficult because no direct visual reference of the beam spot on the cold mirror is present, neither in this setup nor in MicroBooNE. Therefore before closure of the cryostat the cold mirror was aligned such that the laser beam points directly into the detector. With this mirror configuration, the laser beam, when properly aligned onto this mirror, will generate an ionization signal in the detector. The alignment of the laser beam from outside onto this last mirror was verifiable by triggering the readout on laser pulses and checking for a beam signal in the detector. To optimise the beam alignment onto the cold mirror, the alignment of the warm mirror on top of the feedthrough was manipulated while laser pulses were emitted. During this procedure the TPC was readout with each laser pulse to find the optimal configuration of the warm mirror.

First recorded laser ionization tracks introduced by a steerable mirror is presented in Figure 5.4, where the mirror points toward the wireplane. On the x-axes the drift time relative to the wireplane (at $t = 0$ s) is shown and on the y-axes again the wire number is indicated (with 4 mm pitch). In Figure 5.5 the laser beam is directed toward the cathode, where it hits the aluminium surface, here a blob of charge is produced by the photoelectric effect. A clear induction signal followed by collection of the charge on the second wireplane can be observed in this event. A full scan of the detector volume, recording 86 events, was performed. This test successfully showed the laser alignment onto the cold mirror and steering this mirror controlled from outside the cryostat to obtain a full scan of the detector.

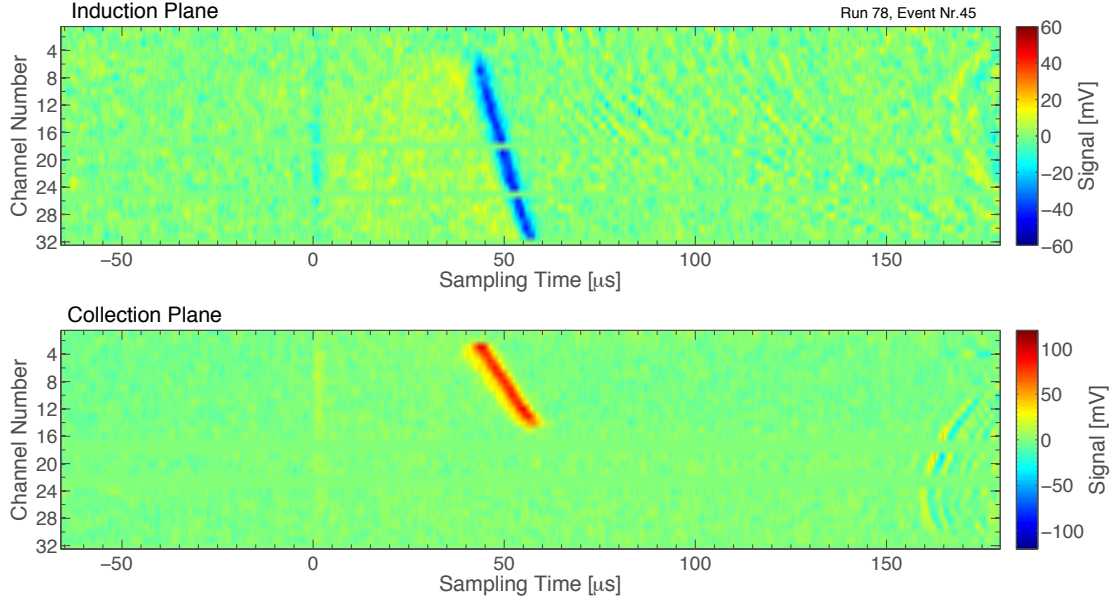


FIGURE 5.4: Laser ionization track in the detector.

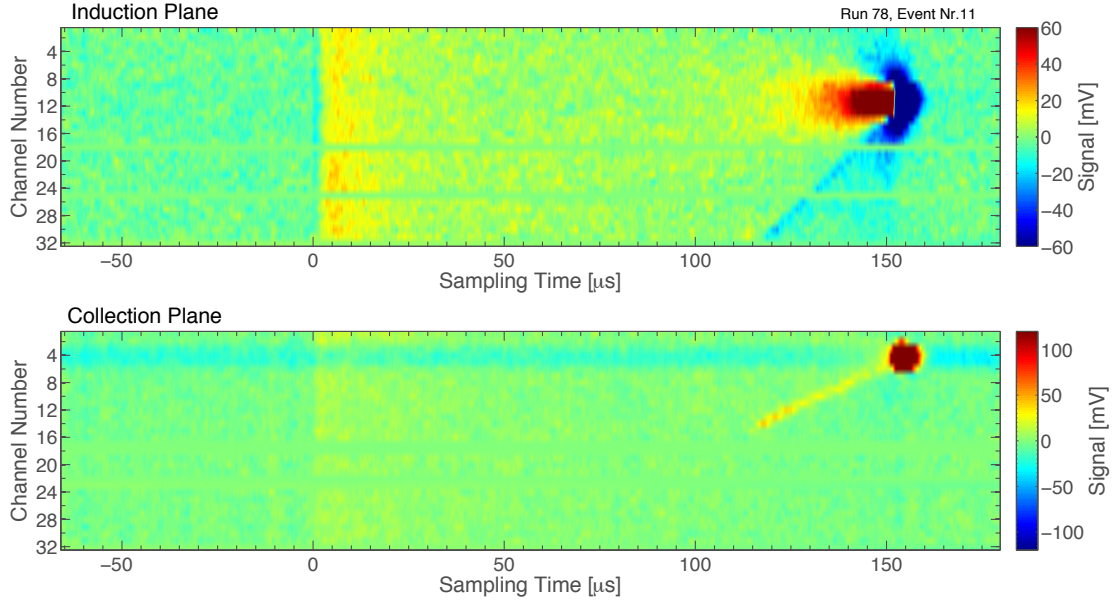


FIGURE 5.5: Laser track towards cathode, hitting cathode and producing a blob of electrons by the photoelectric effect.

5.3 Tests of the Laser Calibration System

The final test includes all parts which will be implemented in the MicroBooNE experiment, the motorised mirror steering as well as position encoding of the two axes. For this test ASIC preamplifiers (see section 4.2) were used for the first time, allowing to record laser ionisation tracks as they will be seen in MicroBooNE. To reduce noise and for protection against damage from breakdowns the amplifier boards were covered with

a copper shielding. Apart from the general proof-of-principle of the laser calibration system, several additional parameters are important to identify for future operation. This includes the scanning speed, positioning accuracy, positioning limits, optimal laser beam energy and diameter and minimal achievable field distortion resolved. These parameters are separately discussed in three categories: position, mirror and detector related. Compared to the previous test no major changes were made with respect to general operation procedures.

Several tests of the motorised feedthrough were performed under warm conditions before the cold test. Crucial parameters for the quality of the electric field calibration is the resolution at which laser tracks can be introduced and measured into the detector. For the rotational axis, the measurement of the angle is done by a ring mounted directly on the movable parts. Therefore this measurement is direct, by means that the measured value is directly related to the measurement position. This is not true for the vertical movement since the linear movement of the bellow is translated into a rotation inside the cryostat, as can be seen in the CAD drawing in Figure 4.5. This construction introduces uncertainties to the measurement position and a backlash. The backlash can be compensated by always approaching positions from the same direction. For the translation of the linear movement ΔL into a rotation $\Delta\phi$ the translation ratio s according to $\Delta L = s \cdot \Delta\phi$ was measured with an laser alignment device¹. A 45° movement was measured by positioning the mirror such that an alignment laser is exactly reflected back, then the mirror was moved 45° such that it overlaps with the laser beam of the alignment device. The obtained ratio is $s = 0.3499 \pm 0.0002 \text{ mm}/{}^\circ$. This translation ratio is used in the following for absolute measurements in the vertical direction. The dominant error in the vertical position measurement is therefore the accuracy of the encoder $\sigma_{linear} = \pm 1 \mu\text{m}$, which translates into a vertical rotation measurement accuracy $\sigma_{vertical} = 10.29''$. Horizontal movement limitations arise from the construction of the feedthrough system, namely the warm mirror support structure. This limit has its origins in the way of mounting the laser table relative to the feedthrough on the MicroBooNE cryostat but had no effect on this test. Vertically the mirror can be rotated more than 45° relative to the horizon in both directions. In an upward looking configuration, no limitations arise which would affect the coverage of the detector with the beam. A limit arises when the mirror faces the opposite downward direction, when properly aligned onto the centre of the mirror the laser diameter and the size of the mirror limits the achievable coverage. However slight misalignment will affect this limit, since the beam will not be in the optimal spot anymore. In warm tests an maximal downward angle of the beam of 37.5° was achieved. For the test presented here the detector was placed inside the detector such that the discussed limits were not reached. Another parameter identified in this test is the maximal movement speed of the cold mirror. The scanning pattern was chosen to scan in horizontal slices, since here the position measurements was not affected by backlash effects. After a slice with linear step size

¹Bosch GPL3.

was obtained the vertical position was increased and a next horizontal slice was scanned. For all scans the starting point was chosen in the upper edge with the mirror facing the cathode. A profile of the encoded vertical (green) and horizontal (blue) scanning pattern is plotted in Figure 5.6. In this test it was found that the laser energy had to be modulated for obtaining optimal tracks (discussed later) in the TPC, but adjustment of the laser energy was not yet automated. For this reason after each horizontal scan, the laser energy was adjusted manually, which introduced a time delay. If automated this would take only seconds and could be performed in parallel with the movement of the vertical axis. Therefore only time scales of the horizontal scan are available. But the missing vertical timescales are very short compared to the total horizontal scanning timescale and are approximated to be 2 s. For each trigger the timestamp was stored for timing analysis in the encoder controller. A horizontal step size of 1.5° and 54 steps were chosen to cover the detector. All 11 horizontal scans took 106 s, resulting in a scanning speed of 2.6 s° for the horizontal plane. The vertical movement was also split into 11 steps, with 2° stepsize, leading to a vertical scanning speed of 1 s° . In total one full scan took 19 minutes and 48 seconds.

The scanning speed and the measurement accuracy might be influenced by the stability of the final setup which has a support structure 3 times longer. Tests in warm of the fully expanded setup showed vibrations if to high speed was chosen. The vibrations might be damped with a more stable fixation in the final setup and the immersion of the setup in liquid argon.

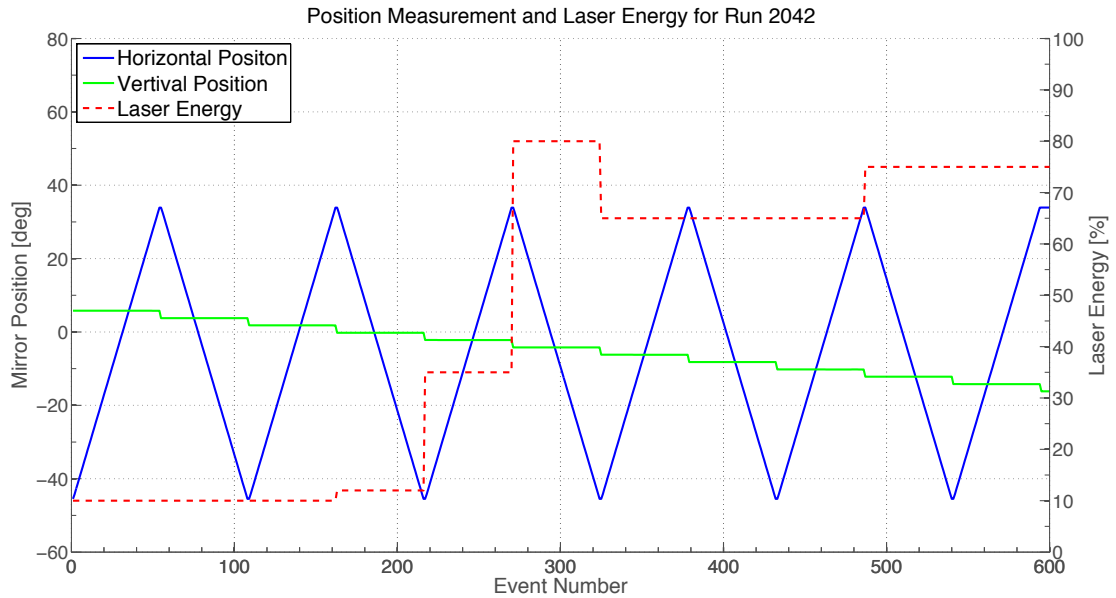


FIGURE 5.6: Recorded position of the cold mirror. For the horizontal position (blue), zero degree is related to a perpendicular track inside the TPC, negative values indicate tracks toward the cathode and positive towards the wireplane. For vertical positions (green) the zero line indicates horizontal tracks, negative values below and positive above the horizon. In red the laser energy relative to the minimum is plotted.

Modulation of the beam energy with respect to the vertical alignment of the cold mirror

was found to be crucial for obtaining sufficient ionisation in the detector. Investigations showed that the reflectivity of the selected dielectric mirrors, which were optimised for 45° , are very sensitive to the angle of incidence (AOI). In Figure 5.6 the laser energy (red line) is plotted for the full scan, the green line indicates the beam angle relative to the horizon (negative (positive) corresponds to downward (upward) looking). In the measurement the laser energy was adjusted to produce similar amounts of collected charge. Before the full scan was conducted a run was dedicated to determine these optimal energies which are displayed in the figure. A clear behaviour is visible in the addressed figure, for AOI lower than 45° the energy needed is nearly constant, at angles slightly higher than 45° the energy strongly increases and stays high for even lower AOI. This behaviour can be explained by the operation principle of the used dielectric mirrors. In this mirror type two types of materials, with high and low refractive index respectively, are stacked. The thickness of the layers is optimised, such that for a certain AOI constructive interference is achieved, going along with a high reflectivity. If now the AOI is changed away from the optimised angle the reflectivity will change accordingly. In air deviations from the optimal AOI do not affect the reflectivity significantly. However in liquid argon the refractive index changes to $n \approx 1.3$ for $\lambda = 266\text{ nm}$ according to [5]. The manufacturer (Edmund Optics) of the used mirrors supplied the simulated reflectivity curves vs. AOI for this configuration which is shown in Figure 5.7. The drop in reflectivity of s-polarised light at around 45° corresponds well with the needed energy increase to obtain laser tracks in the TPC. The main polarisation of the UV-beam is in s-direction since in the attenuator the reflected beam (which is s-polarised) is selected. This finding was not anticipated and will need further investigation and optimisation for the laser calibration system into MicroBooNE.

The emitted UV-laser beam has a diameter of 6 mm and will spatially diverge during propagation, a beam with this diameter will produce an ionization signal larger than the wire spacing. This will certainly limit the capabilities of the full system. With the aperture a small as possible diameter of the laser was selected to enter the detector. Measurements of the diameter were performed with thermal paper (used for thermal printing) on which the selected beam spot burns in. The minimal achieved diameter was 1 mm and was used for further tests.

One of the main goals is to show the feasibility of the laser calibration system to resolve non-uniformities in the electric field, these are introduced by the shortening the field shaping rings 3 and 4 (for details see Figure 4.2). To quantify the expected uniformities in the electric field, a simulation of the homogenous and inhomogeneous electric field was performed. In COMSOL² a 2D axial symmetric simulation of the TPC geometry and the applied voltages on cathode plus field shaping rings was simulated. A cylindric volume with an dielectric constant of $\epsilon = 1.6$ surrounding the detector acted as liquid argon. On the left side of Figure 5.8 the obtained field strength (colour scale) and field lines (black lines) on a surface crossing the TPC are shown, also visible is the detector

²web page: <http://www.comsol.com/>.

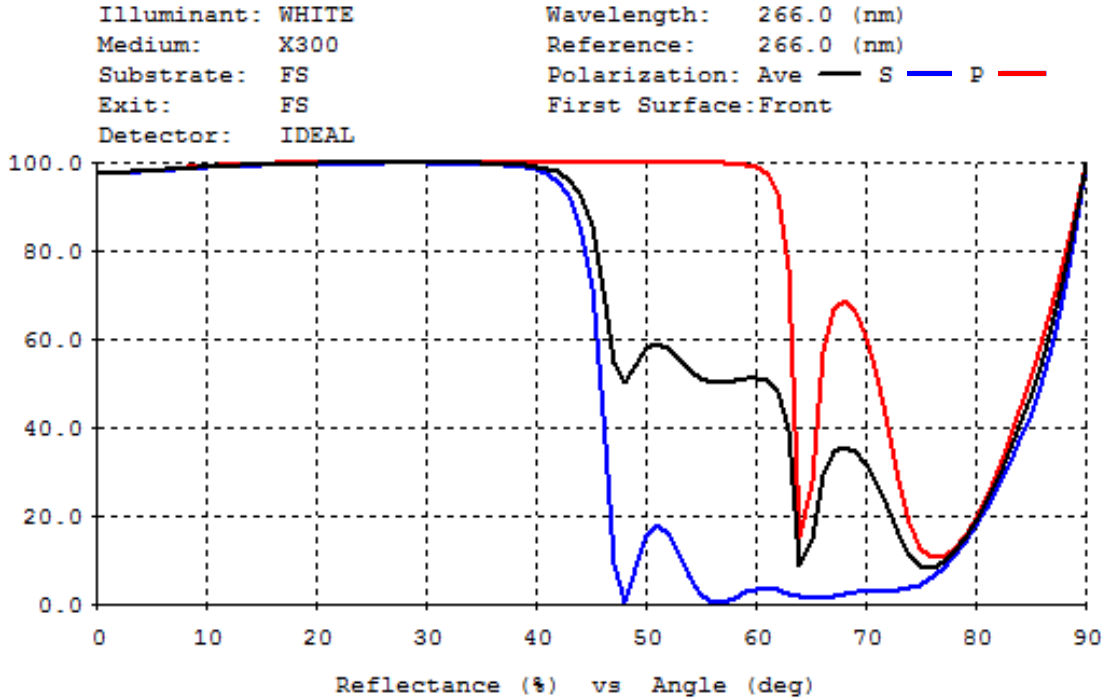


FIGURE 5.7: Simulated reflectivity for s and p polarised light with $\lambda = 266$ nm vs. angle of incidence with surrounding medium with $n = 1.3$. Plot supplied by Edmund Optics.

geometry with the cathode at $z = 0$ mm and the wireplane at $z = 215$ mm. As a measure of the field uniformity the magnitude of the radial field component E_r relative to the axial field component E_z is plotted for different radial cross sections of the detector on the right side of the figure. In the homogenous case a maximal magnitude of 4% is observed at the largest distance to the centre, as well as a modulation of the amplitude due to effects introduced by the field shaping rings. Much stronger variations are observed in the inhomogeneous case. A magnitude of maximally 25% is observable at the outermost distance, which degrades slowly if the radial distance of the cross section is decreased to zero where, because of symmetry, no radial field component is present.

An example laser track of the scanning pattern is shown in Figure 5.9 for the homogenous case. The increased signal to noise ratio compared to previous runs introduced by the cold preamplifiers is visible. From the reading of the high voltage supply and the known resistor chain, the field inside the detector was determined to be $E = 463 \pm 2$ V/cm, using Equation 3.4 the drift time is translated into a drift distance, hence the horizontal axis is changed to drift distance, with the wireplane at 0 mm and accordingly the cathode at the length of the detector $z = 215$ mm. Unfortunately three induction channels broke during operation. In total 594 events were recorded which cover the full volume of the TPC, the stepsize and speed of the scan are described in section 5.3.

With the mirror oriented in the same direction, but shortened rings, tracks were recorded as well, the event view is shown in Figure 5.10. The shape of the distorted beam corresponds well with the expected shape. Entering at approximately 100 mm and leaving the

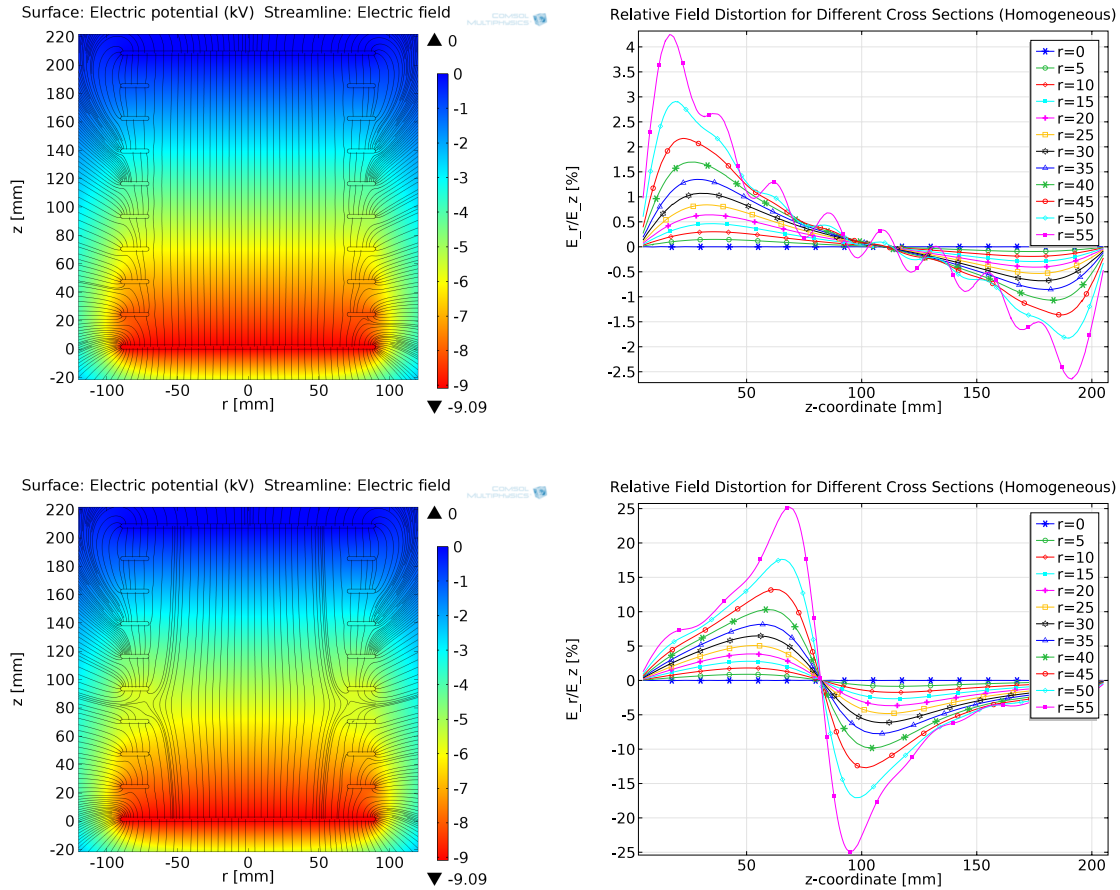


FIGURE 5.8: COMSOL simulation results for the homogenous case (top) and the case with shortened rings 3 and 4 (bottom). On the left side the field strength (colour scale) and field lines (black lines) are shown. On the right side the magnitude of the radial component relative to the axial component of the drift field is plotted for several distances from the origin along the z -axis.

TPC at 140 mm, the beam is mainly bent at in the beginning towards the wireplane and at the ending towards the cathode. The field simulation shows that in this trajectory a higher field than expected for the linear case is present at the entry point, leading to a faster than assumed linear drift. However the electrons produced at the endpoint of the track must travel a longer distance according to the electric field simulation, reaching the wireplane later than assumed for an homogenous field. The field is homogenous in the central regions of the TPC despite the shortened rings, which explains the straight central part of the laser track. Another event with shortened rings is depicted in Figure 5.11, here the laser beam is introduced parallel to the readout plane. Because the cold mirror is situated between the shortened rings and the readout plane the physically parallel track is distorted on both edges in the same direction. Here only the effect of higher field strengths connected to high drift speed is responsible for the track deformed towards the wireplane. The corresponding electric field simulation is confirming this statement. This simulation states a magnitude of a radial field component relative to the axial component of the order of 5% for an drift distance of 80 mm, where the

discussed track is located. This value represents an upper limit for the possible field distortion resolved with the laser calibration system, since a clear bending of the laser track is observable. The resolvable distortions will be lower if laser tracks of greater length can be observed.

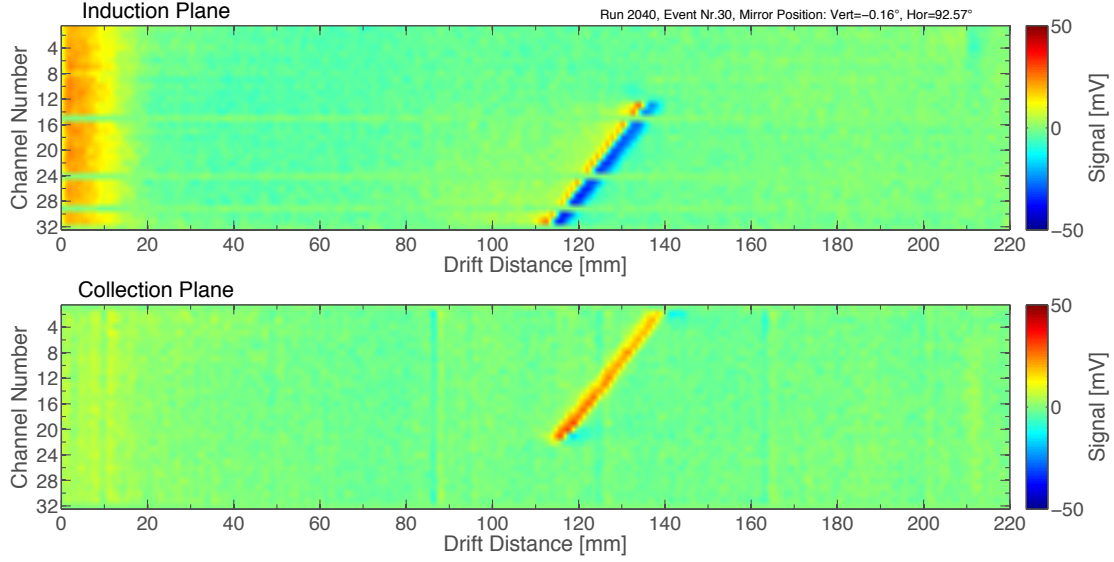


FIGURE 5.9: A laser track inside the TPC facing toward the cathode (at 215mm), measured angles are indicated on the top right.

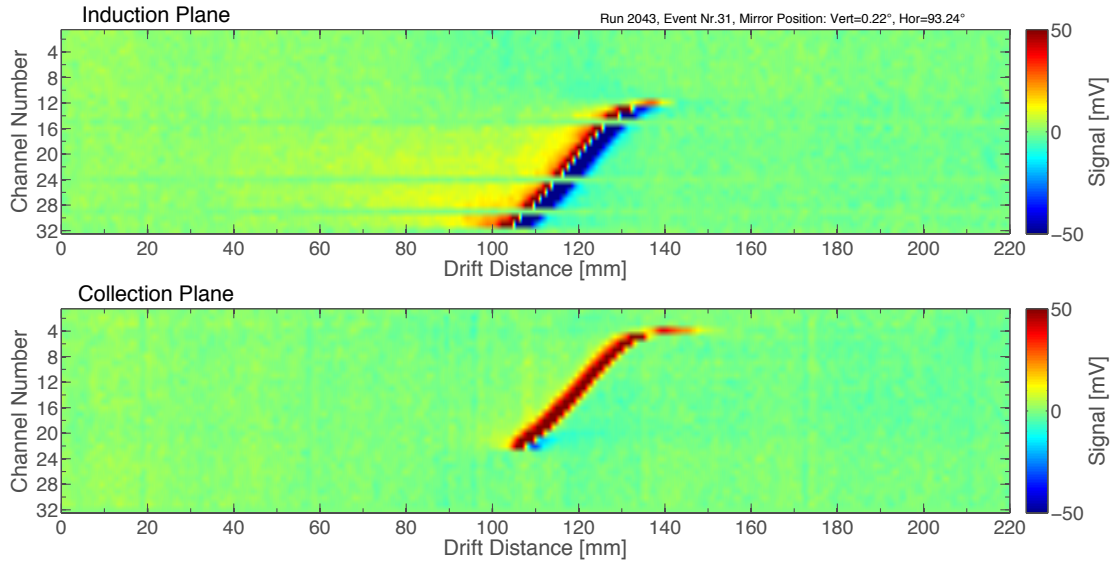


FIGURE 5.10: A laser track with shortened rings 3 and 4 at the approximate same position as Figure 5.9.

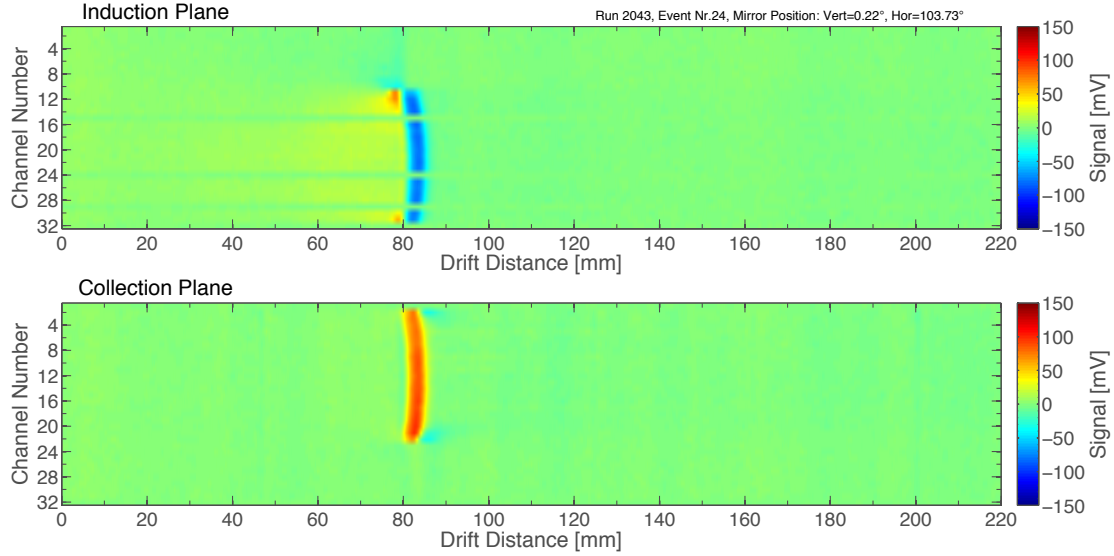


FIGURE 5.11: Distorted laser track parallel to readout plane because of shortened rings.

5.4 Analysis of Collected Laser Tracks

An algorithm to automatically identify laser tracks in the obtained dataset was developed. The motivation behind this is the application of an algorithm which will extract the correction factor from the full set of laser tracks. Main challenges arise from the fluctuations of laser energy, strong noise present in the wire signals, rejection of strong charge signals when the laser hits aluminium support structures and the identification of low signals. Also empty events need to be rejected, since during scanning of the TPC no feedback of successful introduction of laser tracks was implemented. This means that events on which the laser hits a field shaping ring and does not enter the TPC are stored in the dataset too. For the identification of tracks the following procedure was used:

1. Identify corridor where the laser is expected from position measurements.
2. Select all signals above a defined signal strength and below an upper limit.
3. Identify connected patches of signals selected in the previous step and label them.
4. Calculate the weighted (with the wire signal strength) area of the found patches.
5. Select the largest patch and look for peaks on each wire in the selected patch.

The lower threshold in the second step was chosen to eliminate noise present on the wires, the upper limit was chosen in a way that larger than expected signals (produced in photoelectric effect) are not selected. Step three makes use of the fact that laser tracks are connected. For each patch the weighted area is calculated to obtain a criterion on the strength (within the cuts applied) of the signals in the patch. Finally in the patch with the highest signal strength, peaks are searched and connected to a laser trajectory.

A set of identified laser tracks for the homogenous case is shown in Figure 5.12 (top). Only the scan along the horizon was analysed, the full 54 steps were analysed by the above described procedure. In total 30 laser tracks were found, the shadow in the detector introduced by the field shaping rings in front of the cold mirror is clearly visible. A corresponding scan was analysed with shortened rings, the collected tracks are shown in Figure 5.12 (bottom). In comparison fewer tracks were found mainly in the direction towards the cathode. This is a consequence of the decrease of purity between the two scans, they are separated in time by 12 hours. The lower purity implies weaker signals especially for long drift times, these are exactly the tracks missing compared to the homogenous case. An analysis by hand revealed that in the discussed region of the detector tracks are still present but were not included because of the very low signal strength. Ionization signals can be located inside the detector with a resolution of 1.5 mm.

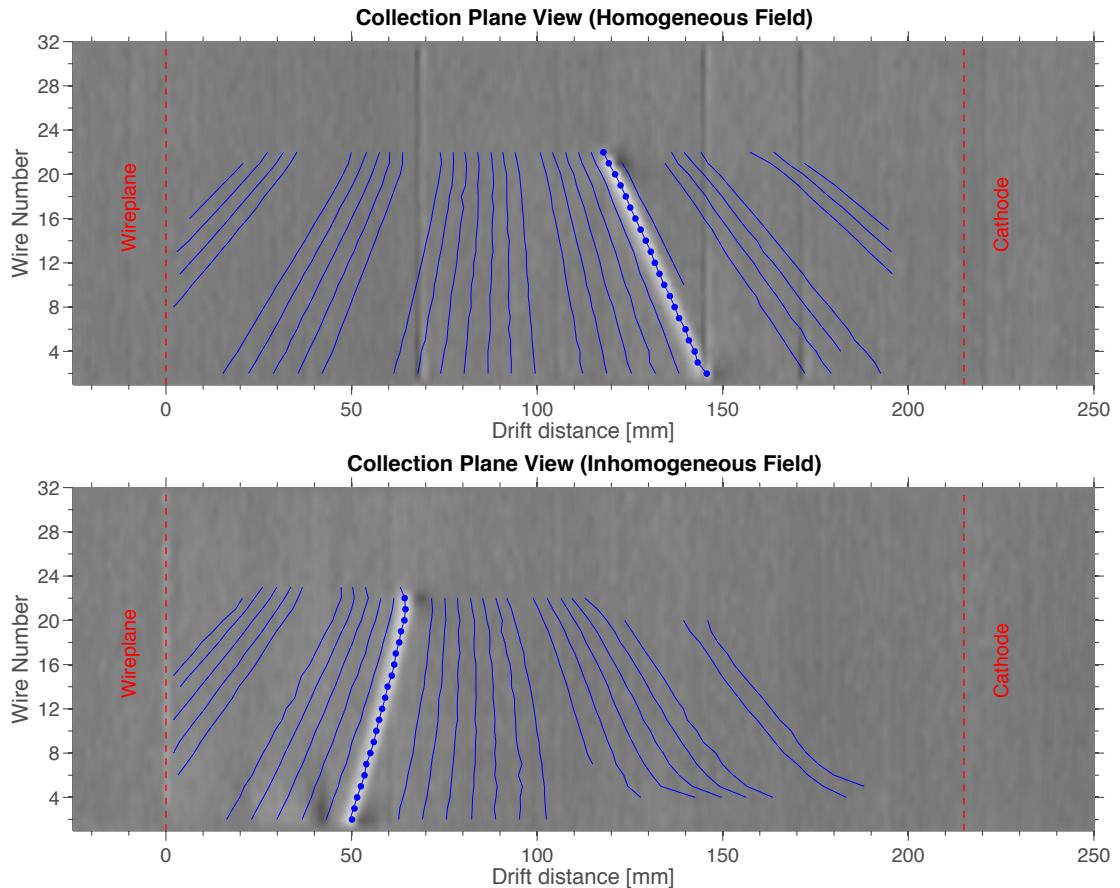


FIGURE 5.12: Collected laser tracks for homogenous (top) and inhomogeneous (bottom) field configuration. The wireplane is situated at a drift distance of 0mm and the cathode at 215 mm. All with the developed algorithm detected tracks are shown, as well as an event display for a example laser track.

5.5 Drift Speed Measurement

The drift speed of the electrons in the TPC is related to the electric field, the higher the field the faster the electrons will traverse the detector. Equation 3.4 expresses an empiric fit to the measured data. For this measurement the laser beam was pointed towards the cathode, in every hit electrons were produced by the photoelectric effect, the time needed for these electrons to reach the readout wires is the drift time t_{drift} . The length of the detector is well known to be $L = 215$ mm. Subsequently the drift speed can be calculated $v_{drift} = L/t_{drift}$ for a given electric field. Supplying different voltages on the cathode allowed to record the drift speed dependant on the electric field. For each electric field configuration 100 shots on the cathode were recorded to reduce the error in the time measurement as well as compensating any fluctuations of the laser energy. Changing only the voltage and keeping the setup otherwise identical leads to consistent results. As can be seen in Figure 3.5 the electron drift speed is also sensitive to temperature. No active measurement of temperature was realised, but since the cryostat was immersed in a bath of liquid argon the temperature of the argon inside the detector volume was assumed to be 89.9 K which is the boiling point of liquid argon. The fact that the liquid argon level dropped very slowly and no bubbles were observable support this assumption.

The lower bound of 0.35 kV/cm of the scanned field strength is due to the effect of the impurity concentration, the longer the electron signal has to travel the more electrons will attach to impurities, diminishing the detectable readout signal until all electrons are absorbed. The upper bound of 0.65 kV/cm was chosen to prevent breakdowns inside the cryostat ensuring no damage was done to the cold preamplifiers. In Figure 5.13 the obtained results are presented, additionally the theoretical fit (blue line) from [41] is shown including the data points (blue squares) on which the fit is based for the region of interest. Another dataset from the ICARUS experiment is shown in green squares. The theoretical fit is dominated by data points well above the here investigated field strength region and is not verified in regions below 0.5 kV/cm. The dominant error for the velocity measurement is the length of the detector of $\sigma_L = 1$ mm, which is connected to the unresolved effect of thermal contraction. The dominant error in determining the electric field strength is the uncertainty in the applied voltage of 0.1%. The presented results lie well within the expected behaviour and are consistent with other measurements.

5.6 Purity Measurement

For future measurements in the cryostat the achieved impurity concentration after filling is of interest. The time evolution of the purity level is dependant on outgassing of the materials present in the detector and hence will be affected by the individual experimental setup. However the outgassing rate is reduced because of the low temperature

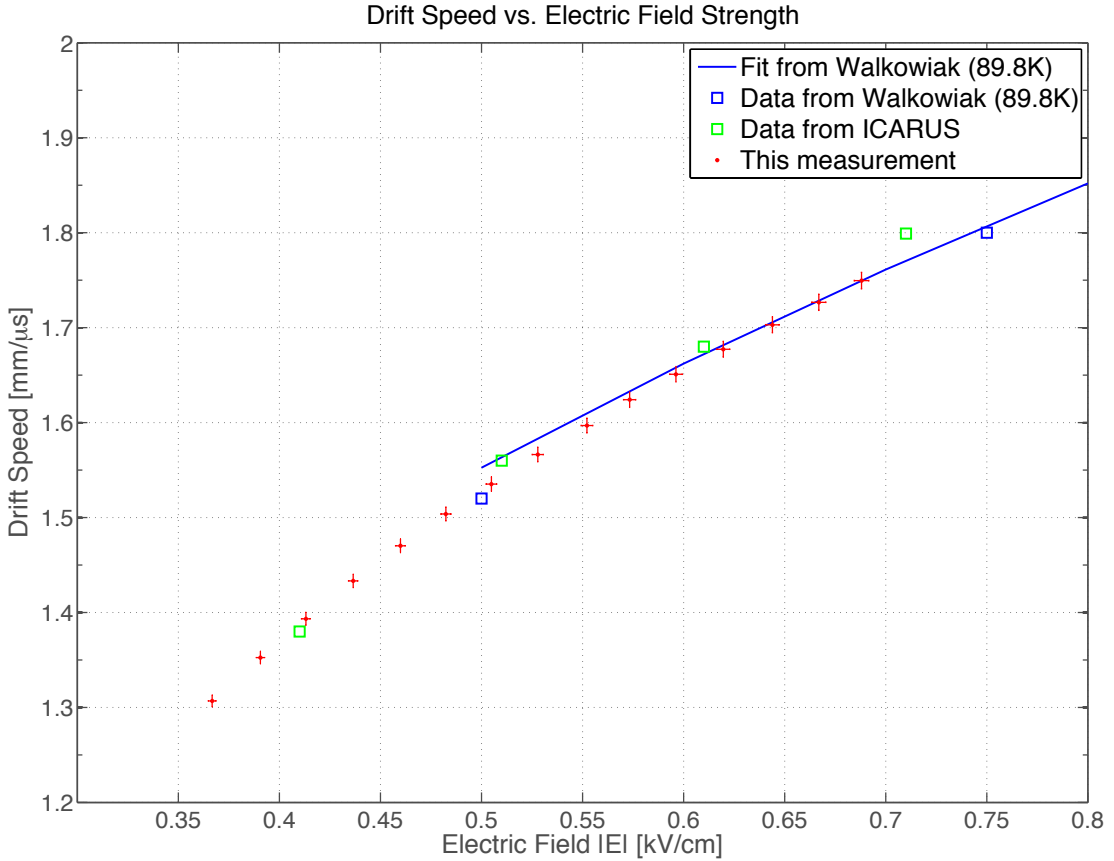


FIGURE 5.13: Measured drift speed as a function of electric field (red points). The blue line depicts the empirical fit from [41] for 89.9 K and blue squares indicate data points on which the fit is based. Data points measured in ICARUS [18] are shown as green squares.

and the purity can be assumed constant for timescales of hours.

To determine the purity level cosmic muons were recorded using the procedure described in section 4.2. Triggering on wires has the disadvantage of only knowing the relative position of the track inside the detector but no absolute position. Otherwise the detector could be deceived in drift distance slices for which the collected charge of a minimum ionizing particle can be measured, which is affected by the impurity concentration according to equation 3.5. To overcome the lack of absolute positioning of a track for argon purity measurement, the attenuation along a single tracks is determined. For this purpose muon tracks that deposit energy constantly as a minimum ionizing particle (2.1 MeV/cm) were selected, this is the case as long as they have enough momentum to traverse the detector. Another criterion is the trajectory, tracks crossing the detector with a high inclination with respect to the azimuth were selected therefore. With this selection long drift distances are covered by a single track.

In a dataset of 11000 cosmic events recorded just after filling, tracks on which the described criteria apply were selected, resulting in 156 events for the attenuation analysis. An example event display of such a track is depicted in Figure 5.14, in the collection

view the attenuation of the signal amplitude (colour scale) is well recognisable. Approximately in the middle of the track a δ -electron is produced, depositing energy in the liquid argon very locally. The wires on which δ -electrons were present were excluded from the analysis. The analysis of the collection signal of the track in figure above is

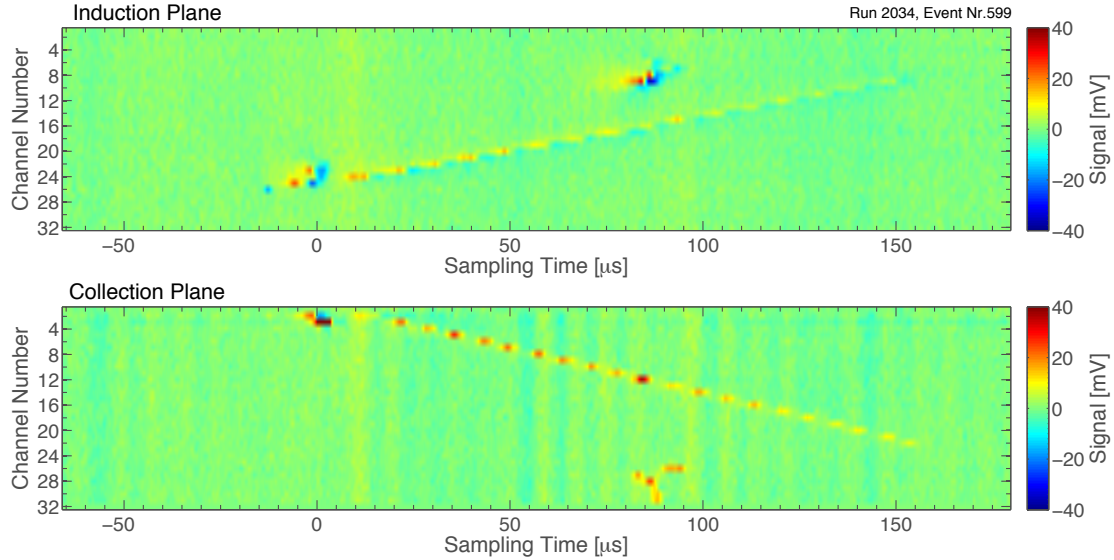


FIGURE 5.14: Example event of a muon crossing with high inclination, approximately in the middle of the track a δ -electron is present.

shown in Figure 5.15. Here the exponential fit to the selected peaks (indicated by blue rings) is overlaid to the wire signals. The wire signals were fitted with an gaussian curve, the peak of the gaussian curve was used for further analysis. To identify the drift time, the centre of the gaussian curve was used. An exponential fit was then used to determine the purity according to this single track. From this set of data a weighted mean was formed which results in a electron lifetime of $\tau_{electron} = 115 \pm 10 \mu s$.

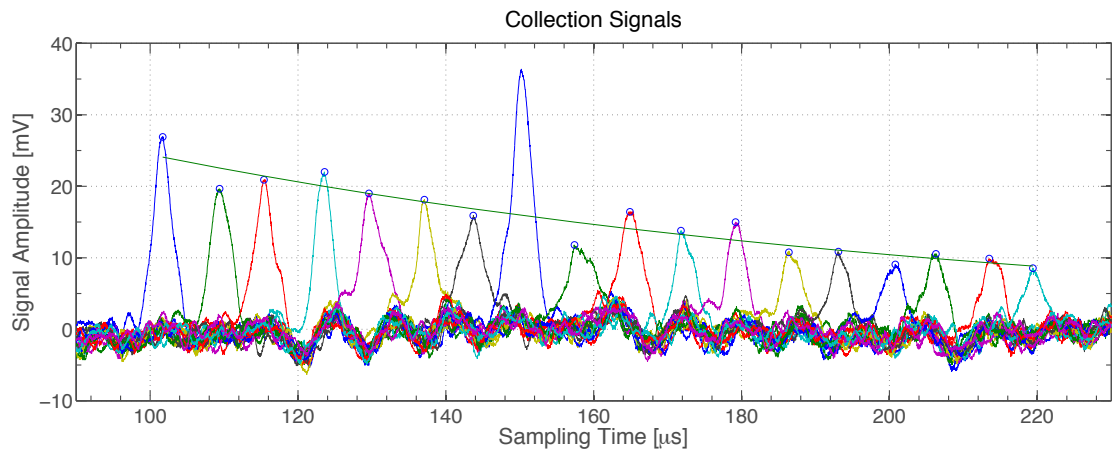


FIGURE 5.15: Wire signals for the relevant wires of event depicted in Figure 5.14. The exponential fit to the maxima is shown as green line, for this analysis a electron lifetime $\tau_{electron} = 117 \pm 15 \mu s$ was found. The strong peak at approximately $150 \mu s$ is due to higher energy deposition by a δ -electron.

5.7 Outlook

Applied onto the geometry of the MicroBooNE detector ($2.3\text{ m} \times 2.5\text{ m} \times 10\text{ m}$), the found measurements accuracy give a laser beam vertical position uncertainty over 10 m of 0.5 mm . The accuracy of the rotary encoder is $\sigma_{horizontal} = 3.2''$, which translates into 0.15 mm measurement accuracy over 10 m in the horizontal direction. Assuming a beam diameter of 1 mm on the cold mirror, the beam spot will be enlarged to 5 mm at 10 m distance, for which the found measurement accuracy is well suited. The identified scanning speeds in this test applied on the proposed scanning volume of $\pm 45^\circ$ horizontally and $\pm 50^\circ$ vertically in MicroBooNE lead to an estimated time for a full scan of 3 hours and 15 minutes. This relatively long time can be significantly reduced by selecting regions of interest, which exist due to the fact that the field shaping rings will generate blind spots for the laser and cannot be scanned at all. Also a significant increase in the resolved field distortion is expected in MicroBooNE since the track length will be up to 10 times longer. The combination of precise laser beam positioning and the positioning resolution of reconstructed laser tracks in MicroBooNE will allow to compensate for the expected space charge effect on position track reconstruction of the order of centimetres (see section 3.3) by a high precision calibration map.

In a next natural step the obtained laser tracks can be used to construct the field calibration map of the TPC. Experimental algorithms for this purpose already exist in the liquid argon group of LHEP. This calibration map can be applied onto the dataset consisting of 1000 cosmic events collected with shortened rings as a cross check and illustration of the capabilities of the system. As the construction of the MicroBooNE detector forges ahead, the equipment used in this test will be sent onsite for installation. The developed software components have to be finalised for the daily operation in the slow control framework of the MicroBooNE experiment.

Chapter 6

Conclusions

The main scope of this Master thesis was to establish the performance and to characterise the laser calibration system designed for the operation on MicroBooNE. In three subsequent steps, the final setup was gradually assembled and the subsystems were ensured to work properly. The first step was dedicated to establish the operation of a liquid argon time projection chamber (LAr TPC), including a vacuum system, cryogenics, the detector itself and data acquisition. In a second step a UV-laser together with an optical table was introduced onto the existing setup, providing a controllable UV-laser beam. This beam was aligned onto a mirror inside the cryogenic environment just in front of the TPC. The mirror was mounted in a structure such that the orientation could be manipulated remotely from outside the cryostat. With this setup for the first time a steerable UV-laser beam was introduced into a LAr TPC. The tests were completed by motorising the movement of the mirror and encoding its precise position. With this final configuration, very similar to the MicroBooNE setup, crucial parameters of the laser calibration system were determined.

Identified position related parameters are the position measurement accuracy of $\sigma_{vertical} = 10.3''$ and $\sigma_{horizontal} = 3.2''$ and the movement speed $v_{vertical} = 2s/\circ$ and $v_{horizontal} = 2.6s/\circ$. It was found that best laser trajectories in the TPC are obtained for a 1mm beam diameter. Additionally the necessity of beam energy modulation depending of angle of incidence on the mirror was identified. In the test detector an artificial radial field distortion could be introduced, the magnitude of the distortion is expressed in the ratio of the desired axial electric field component E_z and the radial distortion component E_r . In the present setup a distortion of $E_z/E_r \approx 5\%$ could be resolved. Furthermore an algorithm to automatically detect laser trajectories in the stored data was developed. In further studies this dataset can be used for performance studies and cross checks of field map reconstruction algorithms.

The successful demonstration of the laser calibration system and the identification of performance parameters lie the basis for daily operation in the MicroBooNE experiment. The high precision laser beam steering in combination with the accurate laser

track reconstruction will allow to compensate for space charge effects in the MicroBooNE detector. The anticipated track position uncertainty of up to 10 cm can be reduced in this way to millimetre-scale.

Appendix A

Photographs of the Setup

Three photographs of the experimental setup are displayed in the following. Figure A.1 shows the UV-laser and the optical table, with (1) the UV-laser, (2) the alignment laser, (3) the first dichroic mirror in the 45° -mount, (4) the attenuator, (5) the aperture, (6) the second dichroic mirror mounted in a remotely steerable mirror mount and (7) the photodiode. In green the laser path is overlaid.

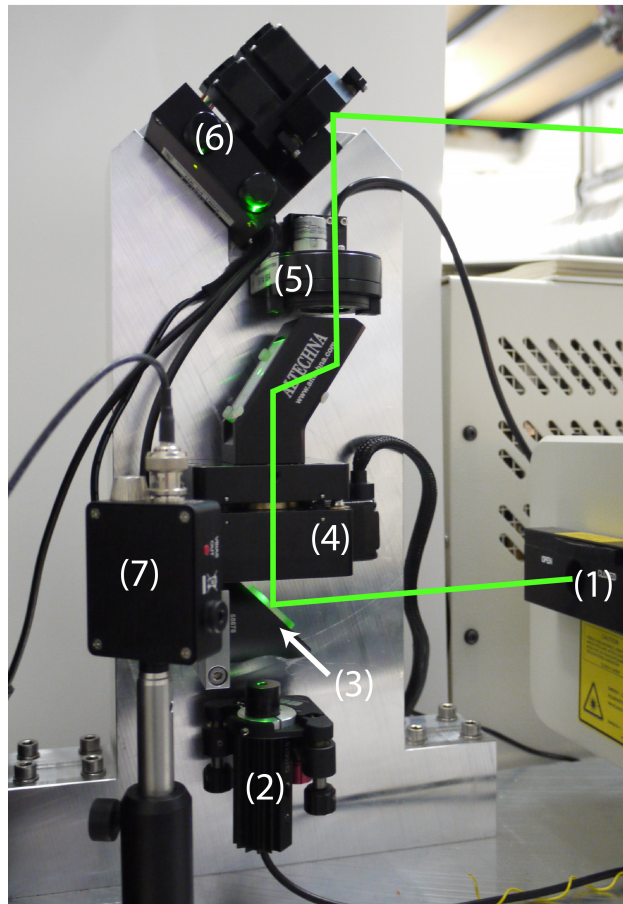


FIGURE A.1: Photograph of the optical table with an overlay of the UV-laser beam path, numbers are discussed in text.

A photograph of the fully assembled laser feedthrough mounted on the cryostat is shown in Figure A.2, here (8) is the last (warm) mirror mounted in a remotely steerable mirror mount, (9) the quartz glass, (10) the linear actuator and encoder and (11) the rotary feedthrough and corresponding encoder.

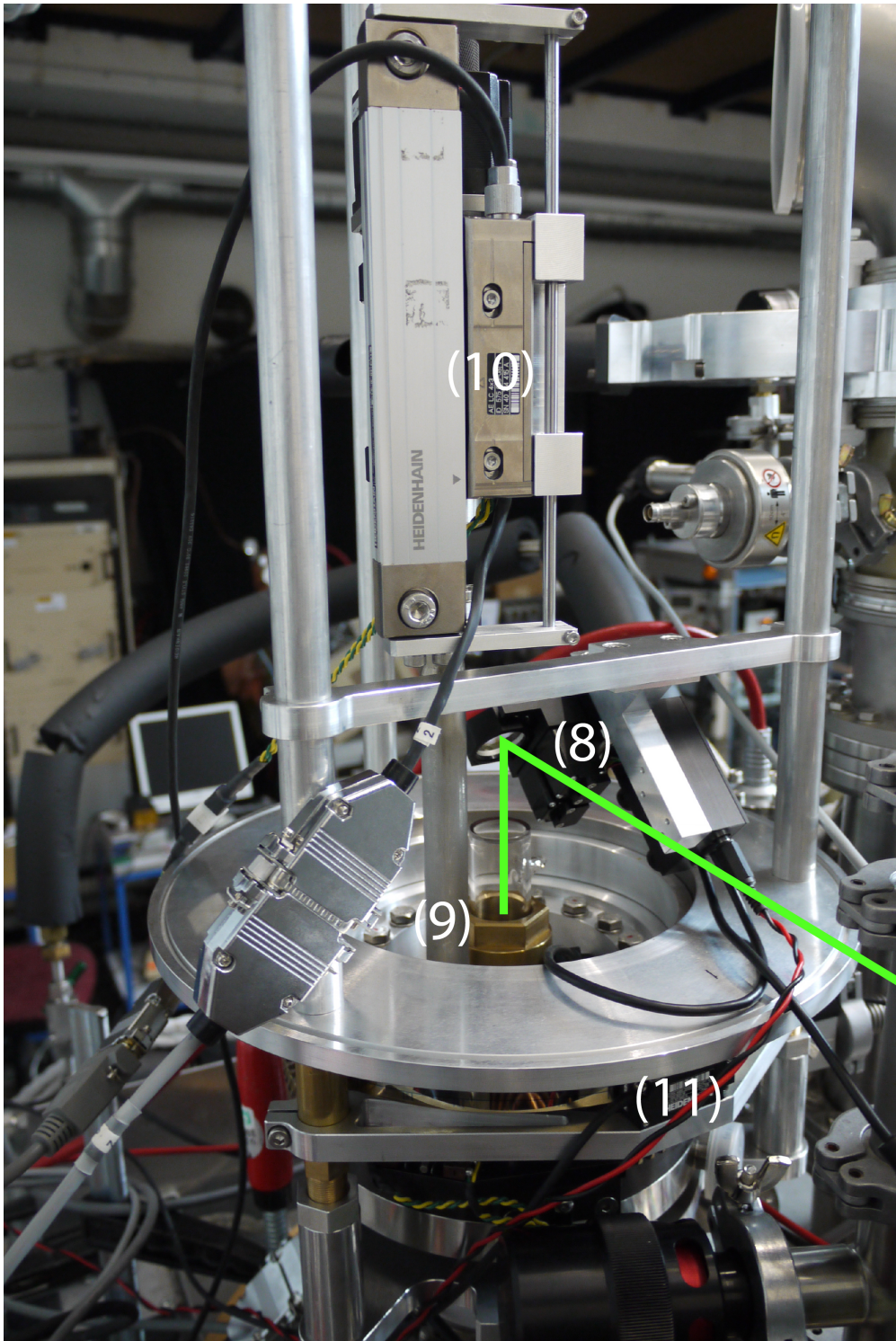


FIGURE A.2: Photograph of the laser feedthrough mounted on the cryostat, description of numbers given in the text.

In Figure A.3 a image of the detector and the cold mirror support structure is depicted. Here (12) is the cold mirror, (13) the field shaping rings and cathode, (14) the wireplanes, (15) the cold amplifiers, (16) the high voltage feedthrough and (17) the shortening device.

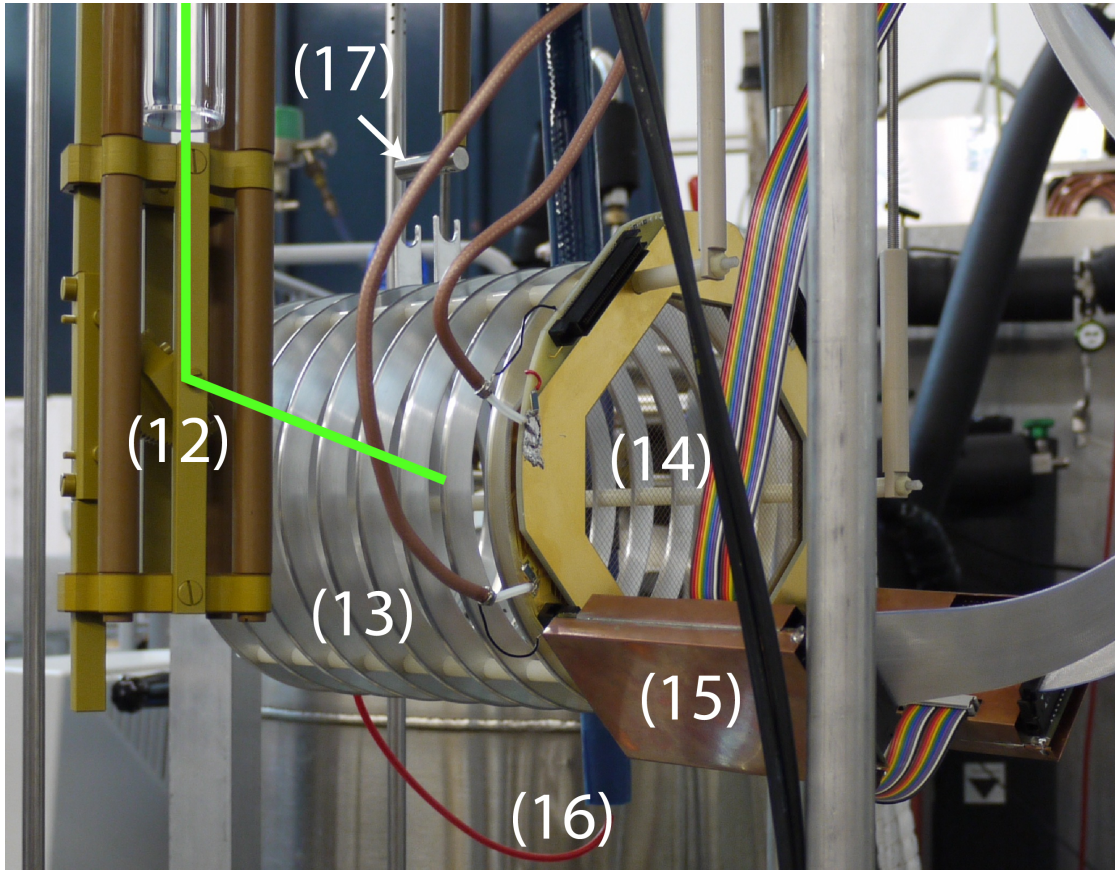


FIGURE A.3: Photograph of the detector and cold mirror support, description of numbers given in the text.

Acknowledgements

I gratefully acknowledge Prof. Antonio Ereditato for initiating and directing this master thesis. I wish to thank my supervisor PD Dr. Igor Kreslo for letting me explore the laboratory freely and his always present support. Furthermore I am also very grateful for the many discussions and guidance by Prof. Michele Weber.

Many thanks go to my fellow students Michael Schenk and Sabina Joss for their friendship and help not only during this thesis work but also the entire study period. For sharing all their invaluable tips and tricks with me and answering all my questions patiently I would like to thank Sébastien Delaquis, Christop Rudolf von Rohr, Dr. Thomas Strauss and Dr. Marcel Zeller. For sharing their TPC design and spare parts I thank the Bern EXO group.

The very familiar atmosphere at LHEP made working very pleasant and encouraging. I appreciate very much the help in construction and design of the mechanical and electronic parts of this thesis by Roger Hänni, Fritz Nydegger, Jan Christen, Roger Liechti, Pascal Lutz and Camilla Tognina.

For enabling my studies in the first place and supporting me over the full period of my studies I am grateful to my parents. I wish to thank my girlfriend Katrin Affolter for supporting me and keeping me sane.

Bibliography

- [1] K. Abazajian, M. Acero, S. Agarwalla, A. Aguilar-Arevalo, C. Albright, et al. Light Sterile Neutrinos: A White Paper. *ArXiv e-prints*, 2012.
- [2] A. Aguilar-Arevalo et al. Evidence for neutrino oscillations from the observation of anti-neutrino(electron) appearance in a anti-neutrino(muon) beam. *Phys.Rev.*, D64:112007, 2001.
- [3] A. Aguilar-Arevalo et al. The MiniBooNE Detector. *Nucl.Instrum.Meth.*, A599:28–46, 2009.
- [4] A. Aguilar-Arevalo et al. Improved Search for $\bar{\nu}_\mu \rightarrow \bar{\nu}_e$ Oscillations in the Mini-BooNE Experiment. *Phys.Rev.Lett.*, 110(16):161801, 2013.
- [5] M. Antonello, F. Arneodo, A. Badertscher, B. Baibusinov, M. Baldo-Ceolin, et al. Detection of Cherenkov light emission in liquid argon. *Nucl.Instrum.Meth.*, A516:348–363, 2004.
- [6] C. Athanassopoulos et al. The Liquid scintillator neutrino detector and LAMPF neutrino source. *Nucl.Instrum.Meth.*, A388:149–172, 1997.
- [7] I. Badhrees, A. Ereditato, I. Kreslo, M. Messina, U. Moser, B. Rossi, M. S. Weber, M. Zeller, C. Altucci, S. Amoruso, R. Buzzese, and R. Velotta. Measurement of the two-photon absorption cross-section of liquid argon with a time projection chamber. *New Journal of Physics*, 12(11):113024, 2010.
- [8] T. M. Collaboration. The MicroBooNE Technical Design Report. Technical report, Fermilab, Feb 2012.
- [9] J. Conrad, C. Ignarra, G. Karagiorgi, M. Shaevitz, and J. Spitz. Sterile Neutrino Fits to Short Baseline Neutrino Oscillation Measurements. *Adv.High Energy Phys.*, 2013:163897, 2013.
- [10] G. De Geronimo, A. D’Andragora, S. Li, N. Nambiar, S. Rescia, E. Vernon, H. Chen, F. Lanni, D. Makowiecki, V. Radeka, C. Thorn, and B. Yu. Front-end asic for a liquid argon tpc. *Nuclear Science, IEEE Transactions on*, 58(3):1376–1385, 2011.

- [11] T. Doke, A. Hitachi, S. Kubota, A. Nakamoto, and T. Takahashi. Estimation of fano factors in liquid argon, krypton, xenon and xenon-doped liquid argon. *Nuclear Instruments and Methods*, 134(2):353 – 357, 1976.
- [12] A. Ereditato, C. C. Hsu, S. Janos, I. Kreslo, M. Messina, C. R. von Rohr, B. Rossi, T. Strauss, M. S. Weber, and M. Zeller. Design and operation of ARGONTUBE: a 5 m long drift liquid argon TPC. *Journal of Instrumentation*, 8:7002P, July 2013.
- [13] J. B. et al. (particle data group). *Phys. Rev. D*, 86(010001), 2012.
- [14] A. Fedenev, A. Morozov, R. Kruescken, S. Schoop, J. Wieser, and A. Ulrich. Applications of a broadband electron-beam pumped xuv radiation source. *Journal of Physics D: Applied Physics*, 37(11):1586, 2004.
- [15] A. Gedanken, J. Jortner, B. Raz, and A. Szoek. Electronic energy transfer phenomena in rare gases. *The Journal of Chemical Physics*, 57(8):3456–3469, 1972.
- [16] C. Giunti. Phenomenology of Sterile Neutrinos. *J.Phys.Conf.Ser.*, 408:012009, 2013.
- [17] A. Hitachi, T. Takahashi, N. Funayama, K. Masuda, J. Kikuchi, and T. Doke. Effect of ionization density on the time dependence of luminescence from liquid argon and xenon. *Phys. Rev. B*, 27:5279–5285, May 1983.
- [18] Icarus Collaboration. Analysis of the liquid argon purity in the ICARUS T600 TPC. *Nuclear Instruments and Methods in Physics Research A*, 516:68–79, Jan. 2004.
- [19] S. F. King and C. Luhn. Neutrino Mass and Mixing with Discrete Symmetry. *Rept.Prog.Phys.*, 76:056201, 2013.
- [20] I. Kreslo, I. Badhrees, S. Delaquis, A. Ereditato, S. Janos, M. Messina, U. Moser, B. Rossi, and M. Zeller. 30 kV coaxial vacuum-tight feedthrough for operation at cryogenic temperatures. *Journal of Instrumentation*, 5:11002, Nov. 2010.
- [21] S. Kubota, M. Hishida, M. Suzuki, and J.-z. Ruan(Gen). Dynamical behavior of free electrons in the recombination process in liquid argon, krypton, and xenon. *Phys. Rev. B*, 20:3486–3496, Oct 1979.
- [22] A. Lebedev. A laser calibration system for the STAR TPC. *Nucl. Instrum. Methods Phys. Res., A*, 478(1-2):163–165, 2002.
- [23] M. Martin. Exciton selftrapping in rare gas crystals. *The Journal of Chemical Physics*, 54(8):3289–3299, 1971.
- [24] J. N. Marx and D. R. Nygren. The time projection chamber. *Print edition*, 31(10):46–53, 1978.

- [25] G. Mention, M. Fechner, T. Lasserre, T. A. Mueller, D. Lhuillier, M. Cribier, and A. Letourneau. Reactor antineutrino anomaly. *Phys. Rev. D*, 83:073006, Apr 2011.
- [26] L. S. Miller, S. Howe, and W. E. Spear. Charge transport in solid and liquid ar, kr, and xe. *Phys. Rev.*, 166:871–878, Feb 1968.
- [27] D. Miskowiec and P. Braun-Munzinger. Laser calibration system for the CERES Time Projection Chamber. *Nucl.Instrum.Meth.*, A593:188–202, 2008.
- [28] M. Miyajima, T. Takahashi, S. Konno, T. Hamada, S. Kubota, H. Shibamura, and T. Doke. Average energy expended per ion pair in liquid argon. *Phys. Rev. A*, 9:1438–1443, Mar 1974.
- [29] E. Morikawa, R. Reininger, P. Guertler, V. Saile, and P. Laporte. Argon, krypton, and xenon excimer luminescence: From the dilute gas to the condensed phase. *The Journal of Chemical Physics*, 91(3):1469–1477, 1989.
- [30] R. S. Mulliken. Potential curves of diatomic rare gas molecules and their ions, with particular reference to xe2. *The Journal of Chemical Physics*, 52(10):5170–5180, 1970.
- [31] S. Palestini, G. Barr, A. Ceccucci, J. Cogan, D. Cundy, et al. Space charge in ionization detectors and the NA48 electromagnetic calorimeter. *Nucl.Instrum.Meth.*, A421:75–89, 1999.
- [32] R. Platzman. Total ionization in gases by high-energy particles: An appraisal of our understanding. *The International Journal of Applied Radiation and Isotopes*, 10(2–3):116–127, 1961.
- [33] G. Renault, B. Nielsen, J. Westergaard, and J. GaardhOJe. The Laser of the ALICE Time Projection Chamber. *Int.J.Mod.Phys.*, E16:2413–2418, 2007.
- [34] C. Rubbia. The liquid-argon time projection chamber: a new concept for neutrino detectors. Technical Report CERN-EP-INT-77-8, CERN, Geneva, 1977.
- [35] S. Schael et al. Precision electroweak measurements on the Z resonance. *Phys.Rept.*, 427:257–454, 2006.
- [36] J. Sun, D. Cao, and J. Dimmock. Investigating laser-induced ionization of purified liquid argon in a time projection chamber. *Nuclear Instruments and Methods in Physics Research Section A: Accelerators, Spectrometers, Detectors and Associated Equipment*, 370(2-3):372 – 376, 1996.
- [37] J. Thomas and D. A. Imel. Recombination of electron-ion pairs in liquid argon and liquid xenon. *Phys. Rev. A*, 36:614–616, Jul 1987.

- [38] C. Thorn, Y. Bo, and G. Mahler. Avoiding TPC Spatial Mapping Errors. Presentation at MicroBooNE Collaboration Meeting, March 2013.
- [39] A. L. Unit and A. Collaboration. Liquid argon calorimeter technical design report. Technical report, CERN, 1996.
- [40] I. Velchev, W. Hogervorst, and W. Ubachs. Precision vuv spectroscopy of ar i at 105 nm. *Journal of Physics B: Atomic, Molecular and Optical Physics*, 32(17):L511, 1999.
- [41] W. Walkowiak. Drift Velocity of Free Electrons in Liquid Argon. Technical Report ATL-LARG-99-008, CERN, Geneva, Jul 1999.

Erklärung

gemäss Art. 28 Abs. 2 RSL 05

Matrikelnummer: 07-916-166

Studiengang: Master in Experimental Physics

Bachelor Master Dissertation

Titel der Arbeit: Design and Test of a Laser Calibration System
for MicroBooNE

Leiter der Arbeit: Prof. Dr. Antonio Ereditato
PD Dr. Igor Kreslo

Ich erkläre hiermit, dass ich diese Arbeit selbstständig verfasst und keine anderen als die angegebenen Quellen benutzt habe. Alle Stellen, die wörtlich oder sinngemäss aus Quellen entnommen wurden, habe ich als solche gekennzeichnet. Mir ist bekannt, dass andernfalls der Senat gemäss Artikel 36 Absatz 1 Buchstabe o des Gesetzes vom 5. September 1996 über die Universität zum Entzug des auf Grund dieser Arbeit verliehenen Titels berechtigt ist.

Bern, den 6. Januar 2014

Lüthi Matthias